

**EXTREME IN-PLANE THERMAL CONDUCTIVITY ANISOTROPY IN  
RHENIUM-BASED DICHALCOGENIDES**

SINA TAHBAZ

A THESIS SUBMITTED TO THE FACULTY OF GRADUATE STUDIES  
IN PARTIAL FULFILMENT OF THE REQUIREMENTS  
FOR THE DEGREE OF  
MASTERS OF SCIENCE

GRADUATE PROGRAM IN ELECTRICAL ENGINEERING & COMPUTER SCIENCE  
YORK UNIVERSITY  
TORONTO, ONTARIO

OCTOBER 2023

© Sina Tahbaz, 2023

# Abstract

Anisotropies in thermal conductivity are important for thermal management in a variety of applications, but also provide insight on the physics of nanoscale heat transfer. As materials are discovered with more extreme transport properties, it is interesting to ask what the limits are for how dissimilar the thermal conductivity can be along different directions in a crystal. In this thesis the thermal properties of Rhenium-based transition metal dichalcogenides (TMDs), specifically Rhenium Disulfide ( $\text{ReS}_2$ ) and Rhenium Diselenide ( $\text{ReSe}_2$ ) are reported, highlighting their extraordinary thermal conductivity anisotropy. Along the basal crystal plane of  $\text{ReS}_2$ , a maximum of  $169 \pm 11$  W/mK is detected along the  $b$ -axis and a minimum of  $53 \pm 4$  W/mK perpendicular to it. For  $\text{ReSe}_2$ , the maximum and minimum values of  $116 \pm 3$  W/mK and  $27 \pm 1$  W/mK are found to lie  $60^\circ$  and  $150^\circ$  away from the  $b$ -axis, along the polarization direction of some of the principal Raman modes. These measurements demonstrate a remarkable anisotropy of  $3.2\times$  and  $4.3\times$  in the conductivity *within* the crystal basal planes, respectively. The through-plane thermal conductivities, recorded at  $0.66 \pm 0.01$  W/mK for  $\text{ReS}_2$  and  $2.31 \pm 0.01$  W/mK for  $\text{ReSe}_2$ , highlight the impact of their layered structures, contributing to notably high in-plane to through-plane thermal conductivity ratios of  $256\times$  for  $\text{ReS}_2$  and  $50\times$  for  $\text{ReSe}_2$ . This research demonstrates the unique thermal properties that

---

these comparatively underexplored TMDs have, shedding light on the need for further exploration into the intricate thermal behavior of such materials, while underscoring their potential significance for future applications in the fields of semiconductor devices and nanotechnology.

# Acknowledgements

I would like to express my deepest gratitude to everyone who supported me throughout the process of completing this thesis. Their assistance, encouragement, and patience were invaluable. First and foremost, I would like to thank my supervisor, Prof. Simone Pisana, for his guidance, patience, and unwavering support. His expertise and insightful feedback was instrumental in shaping my research. I would also like to extend my gratitude to the member of my supervisory committee, Prof. Paul O'Brien, for his valuable suggestions and comments. I would like to acknowledge my fellow lab members and colleagues, particularly Reza, Shany and Olga, for their constructive discussions, collaboration, and camaraderie. My heartfelt thanks go to my family, especially my parents, for their unwavering love, support, and belief in me throughout this journey. I am truly grateful for everyone's contributions and feel fortunate to have had the support of such a wonderful network of people. This work has been supported by the Natural Sciences and Engineering Research Council of Canada, the Canada Foundation for Innovation and the Ontario Research Fund. We are grateful to Prof. Rodney Smith at the University of Waterloo for access to their Raman spectrometer.



# Table of Contents

<b>Abstract</b>	<b>ii</b>
<b>Acknowledgements</b>	<b>iv</b>
<b>Table of Contents</b>	<b>v</b>
<b>List of Tables</b>	<b>vii</b>
<b>List of Figures</b>	<b>viii</b>
<b>1 Introduction</b>	<b>1</b>
1.1 Heat Transport . . . . .	3
1.2 2D Materials . . . . .	6
1.3 Measurement Methods . . . . .	7
1.4 Thesis Structure . . . . .	10
<b>2 Frequency Domain Thermorefectance</b>	<b>12</b>
2.1 Overview . . . . .	12

---

2.2	Modeling . . . . .	15
2.3	Ballistic vs. Diffusive Transport . . . . .	18
2.4	Sensitivity . . . . .	19
2.5	Experimental Setup . . . . .	22
2.6	Spot Size . . . . .	25
2.7	Matlab Code . . . . .	26
2.8	Summary . . . . .	29
<b>3</b>	<b>Beam Offset Frequency Domain Thermoreflectance</b>	<b>32</b>
3.1	Overview . . . . .	32
3.2	Theory . . . . .	33
3.3	Experimental Setup . . . . .	37
<b>4</b>	<b>Anisotropic Thermal Conductivity Measurement in Rhenium Dichalcogenides</b>	<b>42</b>
4.1	Modeling FDTR Data . . . . .	43
4.2	Sample Preparation and Characterization . . . . .	46
4.3	Model Parameters and Sensitivity Analysis . . . . .	52
4.4	Results . . . . .	62
<b>5</b>	<b>Conclusion</b>	<b>70</b>
	<b>References</b>	<b>72</b>

# List of Tables

4.1	List of parameters used in the model for $\text{ReS}_2$ . . . . .	52
4.2	List of parameters used in the model for $\text{ReSe}_2$ . . . . .	52

# List of Figures

2.1	Thermal conductivity sensitivity analysis for Al/SiO <sub>2</sub> /Si sample. The spot sizes of pump and probe beams are 1.5 and 0.8 $\mu\text{m}$ respectively. $k_z$ and $k_r$ refer to the through-plane and in-plane thermal conductivities and the numbers represent the different layers of the sample. . . . .	20
2.2	Detailed representation of the FDTR Setup . . . . .	23
2.3	The FDTR Setup . . . . .	24
2.4	Razor profiling analysis for the pump laser. W in the parameters list is the radius of the beam in micrometers. The horizontal axis is the movement of the sample in micrometers and the vertical axis is the derivative of the laser intensity from the power meter. . . . .	27
2.5	Razor profiling analysis for the probe laser. W in the parameters list is the radius of the beam in micrometers. The horizontal axis is the movement of the sample in micrometers and the vertical axis is the derivative of the laser intensity from the power meter. . . . .	28

---

2.6	Sample fit for the thickness of gold layer on Kapton tape. (a) Fitted thickness and standard error, in meters, (b) Parameter matrix for the 2-layered sample where $\lambda$ and $\lambda_r$ are the through- and in-plane thermal conductivity, and C and t are the volumetric heat capacity and thickness. (c) A plot comparing the measured thermal phase versus frequency (red circles) with the model for the best fit (blue stars).	31
3.1	Sample sensitivity analysis with no offset for Al/ReS <sub>2</sub> . The spot sizes of pump and probe beams are 5.8 and 2.5 $\mu\text{m}$ respectively. K <sub>x</sub> , K <sub>y</sub> , and K <sub>z</sub> refer to the three directions of thermal conductivity and the numbers represent the different layers of the sample. Sensitivities of K <sub>x3</sub> and K <sub>y3</sub> have very similar peaks making them indistinguishable to fit for simultaneously. . . . .	34
3.2	Sample sensitivity analysis for Al/ReS <sub>2</sub> with 3.7 $\mu\text{m}$ offset. The spot sizes of pump and probe beams are 5.8 and 2.5 $\mu\text{m}$ respectively. K <sub>x</sub> , K <sub>y</sub> , and K <sub>z</sub> refer to the three directions of thermal conductivity and the numbers represent the different layers of the sample. The offset separates K <sub>x3</sub> and K <sub>y3</sub> peaks making them distinguishable from each other making it possible to fit for them simultaneously. . . . .	35
3.3	The Beam Offset FDTR Setup . . . . .	37
3.4	Calculating beam offset using razor profiling method . . . . .	38
3.5	Measuring thermal conductivity of graphite using BO-FDTR . . . . .	40
4.1	(a) Optical microscope image of a ReS <sub>2</sub> flake. (b) Optical profilometry thickness measurement of the ReS <sub>2</sub> flake in (a) across the line shown. (c) Crystal structure of ReS <sub>2</sub> . . . . .	48

---

4.1	(d) In-plane and through-plane thermal conductivity of ReS <sub>2</sub> for different angles. The 0° axis is aligned with the bottom edge of the flake in (a). (e) Polarized Raman spectroscopy of the ReS <sub>2</sub> flake for different rotations of the crystal with the 0° angle aligning the bottom edge of the flake in (a) to the polarization axis of the Raman laser. (f) Polar plot of the Raman intensities for the 5 dominant modes of ReS <sub>2</sub> shown in (e).	49
4.2	(a) Optical microscope image of a ReSe <sub>2</sub> flake. (b) Optical profilometry thickness measurement of the ReSe <sub>2</sub> flake in (a) across the line shown. (c) Crystal structure of ReSe <sub>2</sub> .	50
4.2	(d) In-plane and through-plane thermal conductivity of ReSe <sub>2</sub> for different angles. The 0° axis is aligned with the bottom edge of the flake in (a). (e) Polarized Raman spectroscopy of the ReSe <sub>2</sub> flake for different rotations of the crystal with the 0° angle aligning the bottom edge of the flake in (a) to the polarization axis of the Raman laser. (f) polar plot of the Raman intensities for the 4 dominant modes of ReSe <sub>2</sub> shown in (e).	51
4.3	Sample model fit for ReS <sub>2</sub> @30° fitting for K <sub>xx</sub> , K <sub>yy</sub> , and K <sub>zz</sub>	53
4.4	Sample model fit for ReSe <sub>2</sub> @120° fitting for K <sub>xx</sub> , K <sub>yy</sub> , and K <sub>zz</sub>	54
4.5	Thermal Conductivity Sensitivity analysis for ReS <sub>2</sub> . x, y, and z refer to the direction of thermal conductivity and the numbers represent the layer as described in Table 4.1.	56

---

4.6	Variables Sensitivity analysis for $\text{ReS}_2$ . C refers to the volumetric heat capacity of each layer denoted by the numbers and h represents the thickness of each layer as described in Table 4.1. . . . .	57
4.7	Spot Size Sensitivity analysis for $\text{ReS}_2$ with $R_{pp}$ being the radius of the pump beam and $R_{pr}$ the radius of the probe beam. . . . .	58
4.8	Thermal Conductivity Sensitivity analysis for $\text{ReSe}_2$ . x, y, and z refer to the direction of thermal conductivity and the numbers represent the layer as described in Table 4.2. . . . .	59
4.9	Variables Sensitivity analysis for $\text{ReSe}_2$ . C refers to the volumetric heat capacity of each layer denoted by the numbers and h represents the thickness of each layer as described in Table 4.2. . . . .	60
4.10	Spot Size Sensitivity analysis for $\text{ReSe}_2$ with $R_{pp}$ being the radius of the pump beam and $R_{pr}$ the radius of the probe beam. . . . .	61
4.11	Analysis of fitted parameter dependency for $\text{ReS}_2$ at $0^\circ$ orientation alongside the 68% and 95% confidence intervals for the obtained measurement. . . . .	65
4.12	Analysis of fitted parameter dependency for $\text{ReS}_2$ at $120^\circ$ orientation alongside the 68% and 95% confidence intervals for the obtained measurement. . . . .	66
4.13	Analysis of fitted parameter dependency for $\text{ReSe}_2$ at $0^\circ$ orientation alongside the 68% and 95% confidence intervals for the obtained measurement. . . . .	67
4.14	Analysis of fitted parameter dependency for $\text{ReSe}_2$ at $120^\circ$ orientation alongside the 68% and 95% confidence intervals for the obtained measurement. . . . .	68

---

4.15 Calibration test fitting for the thickness of the SiO <sub>2</sub> layer in the Al/SiO <sub>2</sub> /Si sample with a known thickness of 150nm. . . . .	69
---	----



# Chapter 1

## Introduction

Transition metal dichalcogenides (TMDs) are a diverse and promising group of two-dimensional (2D) materials that manifest semiconducting properties [1]. Composed of a transition metal (e.g., Molybdenum (Mo), Tungsten (W), or Rhenium (Rh)) and a chalcogen atom (Sulfur (S), Selenium (Se), or Tellurium (Te)), TMDs have invoked considerable scientific interest owing to their unique and often tunable electronic and optical properties, with applications envisioned in optoelectronic and energy harvesting devices [2]. Extensive research has been conducted on the thermal properties of TMDs [3–8] such as  $\text{MoS}_2$  and  $\text{WS}_2$ . Common features of the thermal conductivity of TMDs include high anisotropy with larger thermal conductivity along the basal plane of the layered crystal, due to the weaker bonds found across the plane, lower conductivities for TMDs composed of heavier chalcogen atoms, and long phonon mean free paths at room temperature. Rhenium-based TMDs, specifically  $\text{ReS}_2$  and  $\text{ReSe}_2$ , have received considerably less attention. While the thermal conductivity of  $\text{ReS}_2$  has been investigated by Jang et al [9],  $\text{ReSe}_2$  remains largely unexplored

experimentally. A defining characteristic of  $\text{ReS}_2$  and  $\text{ReSe}_2$  is their crystal structure, being triclinic with a more complex unit cell and hence less symmetric than the more common hexagonal TMD crystal configurations. The lack of crystal symmetry naturally leads to more complex anisotropies. Indeed, Jang et al. [9] measured  $\text{ReS}_2$  to have a thermal conductivity along the Re atomic chains (along the  $b$ -axis) to be  $1.4\times$  larger than the orthogonal in-plane direction, and  $130\times$  larger than the through-plane direction.

Theoretical studies of the thermal properties of both of these materials have been very limited thus far. Tongay et al. [10] performed density functional theory (DFT) calculations of the structure and phonon dispersion of  $\text{ReS}_2$ , showing how the layers constituting the bulk crystal are unusually decoupled, leading to estimated values of thermal conductivity 70 W/mK in-plane and very low conductivity of 0.05 W/mK through the plane. In the case of  $\text{ReSe}_2$ , a study by Mahmoud et al. [11] reports a thermal conductivity of approximately 18 W/mK in the  $a$ -axis and 0.69 W/mK along the  $c$ -axis. Bang et al. [12] instead reports theoretical values of about 9 W/mK in-plane and 2 W/mK through-plane. None of these theoretical studies report any appreciable in-plane anisotropy, in contrast to the experimental results of Jang et al [9].

This work aims to further elucidate on the thermal conductivity of these TMDs. As it will be shown later, a significant observation from this study is the distinctively high in-plane anisotropy manifested by both  $\text{ReS}_2$  and  $\text{ReSe}_2$ , which is a record in comparison to other TMDs and 2D materials in general.

## 1.1 Heat Transport

Heat transport, or the movement of thermal energy from one place to another, is a fundamental physical phenomenon of significant importance. It underpins many of the scientific principles and technological advancements that define modern society. From the operation of simple heat engines to the development of cutting-edge nanoelectronics, understanding heat transport can provide the insights necessary to push the boundaries of scientific and technological possibilities.

When heat transport is discussed, it is essentially referring to the energy transfer resulting from a temperature difference within a system or between different systems. According to the second law of thermodynamics, energy naturally flows from regions of higher temperature to regions of lower temperature, seeking to achieve thermal equilibrium. This simple yet profound principle governs the dynamics of heat transport and gives rise to the diverse ways heat is transferred, such as conduction.

Among the mechanisms of heat transport, conduction is crucial, especially in the context of solids. Conduction is the process whereby heat is transferred through the microscopic collision of particles, which can be atoms, molecules, or in the case of metals, free electrons. In this process, kinetic energy is transferred from one particle to another without any large-scale motion of the medium itself.

For crystalline materials, heat conduction is primarily facilitated by lattice vibrations, commonly referred to as phonons [13]. The efficiency with which phonons can transport heat within a material is indicated by a property known as thermal conductivity. A higher thermal conductivity signifies a greater ability to conduct heat. This phonon-mediated heat conduction is influenced by various factors, such as the material's crystal structure, defect density, inherent anisotropy, and temperature,

among others [14]. In the context of thermal conductivity, there is the concept of anisotropy, referring to the fact that not all materials have a uniform thermal conductivity in all directions. Depending on their crystal structure or types of forces between the atoms, some materials can have anisotropic thermal conductivities, meaning they conduct heat in some directions, along a specific atomic chain for instance, at a higher rate compared to other crystal directions.

However, things get even more interesting moving into the realm of nanoscale systems. Here, the classical theories of heat transport, which adequately describe bulk materials, struggle to explain the phenomena observed. For instance, Fourier's law of heat conduction, which assumes that the heat flux within a material is proportional to the negative gradient of the temperature, begins to break down when the system size becomes comparable to the mean free path of the heat carriers, i.e., the phonons or electrons [15]. In these conditions, heat conduction starts to exhibit ballistic or non-diffusive characteristics, challenging the conventional understanding of heat transfer.

Ballistic transport refers to the condition where phonons or electrons travel unhindered, without scattering, over a significant portion of the system, resulting in a direct heat transfer between the hot and cold regions [16]. Conversely, in diffusive or non-ballistic transport, phonons or electrons scatter frequently, causing the heat to spread out in the medium. The transition between these two regimes, and the understanding of their underlying physics, is a topic of active research in the field of heat transport.

Recent years have seen an upsurge in the exploration of heat transport in two-dimensional (2D) layered materials like graphite and transition metal dichalcogenides (TMDs) [17]. These materials are different from 2D materials like graphene in that they consist of atom thin layers

building up their bulk crystal structure. They exhibit unique thermal properties, largely stemming from the different type of bonding between the layers compared to the forces holding the atoms together inside each layer. This causes vastly different thermal conductivities and large anisotropies between the in-plane and through-plane directions. In-depth knowledge of heat transport in these materials can lead to breakthroughs in several application areas, including nanoscale thermal management in semiconductor devices, thermoelectric energy conversion, and advanced thermal barrier coatings [18].

Understanding these novel transport phenomena is achieved through a combination of innovative experimental techniques, advanced theoretical models, and state-of-the-art computational methods. Experimental techniques like time-domain thermoreflectance (TDTR) and frequency-domain thermoreflectance (FDTR) enable precise measurement of thermal properties with extraordinary spatial resolution. Meanwhile, theoretical and computational methods, grounded in quantum mechanics and statistical physics, provide the tools necessary to model and predict heat transport behavior at the atomic level.

In conclusion, the study of heat transport serves as a bridge linking fundamental scientific principles with practical applications in engineering and technology. Our increasing ability to understand and manipulate heat transport at the nanoscale is about to make a revolution in materials science, enabling the design and creation of devices with tailored thermal properties. The exploration of phonon behavior, the understanding of ballistic and diffusive transport regimes, and the investigation of 2D materials contribute to an enriching and expanding field. As the intricacies of heat transport continue to unravel, new opportunities are unlocked for energy management and

technological innovation, propelling us into an era where thermal phenomena are harnessed for the benefit of various applications, from efficient power generation to high-performance computing systems.

## 1.2 2D Materials

Two-dimensional (2D) materials, with their unique physical and chemical properties, have sparked a surge of scientific interest [17]. As their name implies, these materials are characterized by having layers with a thickness of just a few atoms. This ultra-thin configuration of layers gives rise to a host of unique characteristics [19], including electronic, mechanical, and thermal properties, which make these materials promising for various applications [20,21].

The advent of graphene—a single layer of carbon atoms arranged in a two-dimensional honeycomb lattice—announced the arrival of 2D materials, demonstrating an impressive array of properties such as high electrical conductivity, robust mechanical strength, and superior thermal conductivity [22]. The exploration of graphene opened the door to a broader investigation into the family of 2D materials.

Beyond graphene, the spectrum of 2D materials is vast and varied [23], including semiconducting transition metal dichalcogenides (TMDs), insulating hexagonal boron nitride, and several others. Each class of 2D materials boasts unique attributes, making them appealing for a diverse set of applications, from electronics and optoelectronics to energy storage, sensing, and more [24].

Among these, transition metal dichalcogenides (TMDs) have drawn considerable attention [1]. These materials are composed of a transition metal atom (such as Molybdenum, Tungsten, or

Rhenium) sandwiched between two chalcogen atoms (Sulfur, Selenium, or Tellurium), forming a MX<sub>2</sub> structure. Unlike graphene, which is a zero-gap semiconductor, many TMDs exhibit semiconducting properties with band gaps in the visible spectrum, rendering them suitable for applications in electronics and optoelectronics [25].

One particularly compelling aspect of TMDs is the strong correlation between their physical properties and layer number [10]. Single-layer TMDs, for instance, exhibit direct band gaps, making them interesting candidates for optoelectronic devices.

In this study, the focus is on a subset of TMDs involving Rhenium (Re), specifically Rhenium Disulfide (ReS<sub>2</sub>) and Rhenium Diselenide (ReSe<sub>2</sub>). ReS<sub>2</sub> has the unique characteristic of having a direct band gap of 1.5eV in both the bulk and mono layer form [9], making it a suitable candidate for electronic devices and photodetectors. While a significant amount of research has been conducted on other TMDs, most of them showing anisotropic thermal conductivities, Rhenium-based TMDs have been less explored, presenting an opportunity to uncover new insights. In particular, the aim is to investigate their thermal properties, which are crucial for potential applications in electronics where heat management is key. By developing a comprehensive understanding of the thermal conductivities of these Rhenium-based TMDs, I hope to pave the way for their potential use in future devices.

## 1.3 Measurement Methods

Estimating the thermal conductivity of materials is crucial in several fields, such as electronics, thermal management, and material science. Various methods have been developed and refined

over time, each with its unique features, advantages, and challenges. This section will discuss two of the most commonly used methods to measure thermal conductivity of thin films, time-domain thermoreflectance (TDTR) and frequency-domain thermoreflectance (FDTR).

TDTR [26] is a non-contact, pump-probe technique that has been extensively used in recent years to measure the thermal conductivity of thin films and nanostructured materials. The method involves heating the surface of a sample with a pulsed laser (pump beam) and probing the resulting surface temperature change using a delayed probe beam. The probe beam's intensity change upon reflecting from the surface, which depends on the surface temperature, is recorded as a function of the delay time between the pump and probe pulses. This information, along with a thermal model that takes into account the layered structure of the sample and the pump modulation frequency, can be used to determine the thermal conductivity of the material.

One of the advantages of TDTR is its capability to measure the thermal conductivity of very thin films—down to several nanometers thick. This makes it a suitable technique for investigating the thermal properties of many electronic and thin film materials, and in particular 2D materials.

Similar to TDTR, FDTR [27] is a laser-based, non-contact method used to measure the thermal conductivity of materials. However, instead of analyzing the time-delayed reflectance of a probe beam, FDTR involves monitoring the phase and amplitude of the thermoreflectance signal at different modulation frequencies of the pump beam. This frequency sweep provides a more detailed picture of the thermal response of the sample, which can improve the accuracy of the thermal conductivity measurements, particularly for multi-layered samples or materials with anisotropic or depth-dependent thermal properties. It is important to note that without limitations in



the experimental implementation, TDTR performed with high temporal resolution and spanning a large range of pump-probe delay times, is complementary to FDTR performed on a broad frequency bandwidth. In essence, TDTR measures the impulse response function of a system, whereas FDTR measures the frequency-dependent transfer function. In practice, due to different experimental conditions, limitations of the equipment and cost considerations, TDTR and FDTR remain complementary but independent techniques that can be chosen according to the sample being studied and experimental range of interest. A variation of FDTR named Beam Offset FDTR which will be explored in detail in the following chapters is specifically beneficial in my measurements due to the higher sensitivity to in-plane anisotropy making it suitable for the rhenium samples. FDTR also boasts the ability to measure very thin films, like TDTR, and it often provides higher signal-to-noise ratios because the measurement is taken at a steady state. Nevertheless, similar to TDTR, FDTR requires precise control of experimental parameters and careful interpretation of data using appropriate thermal models.

Several other methods exist for measuring thermal conductivity [28], each suitable for specific types of materials or applications. For instance, the 3-omega method [29] is widely used for insulating thin films having low thermal conductivity, based on the measurement of the temperature oscillation amplitude in a metal line deposited on the sample, when an alternating current is applied. The hot-wire method [30], on the other hand, is suitable for fluids and soft porous materials and is based on monitoring the temperature rise of a wire heated by an electrical current and immersed in the sample. Lastly, the laser flash method [31] measures the thermal diffusivity of bulk materials by analyzing the temperature response on the rear face of a sample, following a heat pulse on the front

face.

In summary, the measurement of thermal conductivity involves a variety of techniques, each with its strengths and limitations. The choice of method depends on the nature of the sample (e.g., its thickness, structure, and thermal properties), the required accuracy, and the specific details of the application. Despite the ongoing development and refinement of these techniques, the accurate determination of thermal conductivity, particularly in nanostructured materials and thin films, remains a challenging task, underscoring the need for continual research in this area.

## **1.4 Thesis Structure**

This thesis is structured to provide a comprehensive overview of the methods, experiments, and results associated with the thermal conductivity measurements of the dichalcogenides of Rhenium.

Chapter 2 delves into the fundamentals of Frequency-Domain Thermoreflectance (FDTR). This non-contact, laser-based method is commonly used for measuring the thermal conductivity of materials, and understanding its underlying principles is crucial for the interpretation of the results obtained in later chapters. This section will explain the nuances of FDTR, discuss its advantages, challenges, and typical applications.

In Chapter 3, the discussion is further narrowed down to focus on the Beam Offset Frequency-Domain Thermoreflectance (BO-FDTR) technique. This variant of FDTR offers additional insights into the in-plane thermal properties of anisotropic materials, which can be particularly useful for studying the Rhenium dichalcogenides. This chapter will elaborate on the principles of BO-FDTR, how it differs from conventional FDTR, and how it can provide a more detailed picture of the thermal

behavior of the materials under study.

Chapter 4 constitutes the experimental portion of the thesis. It covers the preparation and execution of the experimental measurements of the thermal conductivity of Rhenium Disulfide ( $\text{ReS}_2$ ) and Rhenium Diselenide ( $\text{ReSe}_2$ ) using the methods discussed in the previous chapters.

Chapter 5 serves as the core section where the actual results and discussion take place. The data obtained from the experiments will be presented, followed by an in-depth discussion and interpretation of these results.

Finally, Chapter 6 concludes the thesis, summarizing the key findings and their implications.

This study aims to fill critical gaps. Firstly, I will conduct an experimental measurement of  $\text{ReSe}_2$ 's thermal conductivity for the first time, providing much-needed empirical data on this TMD. Secondly, I will reevaluate the thermal properties of  $\text{ReS}_2$ , utilizing a different methodology than prior studies. My measurements show a record high anisotropy in both of the materials. In the case of  $\text{ReS}_2$ , the measured anisotropy is even higher than previous studies on this material. This twofold approach will not only broaden the understanding of Rhenium dichalcogenides but also critically examine the impact of experimental methods on the measurement of these properties. Through this, I seek to offer a more comprehensive picture of the behavior and potential applications of these under-studied TMDs.

## **Chapter 2**

# **Frequency Domain Thermoreflectance**

### **2.1 Overview**

Frequency Domain Thermoreflectance (FDTR) is a non-destructive, optical pump-probe technique for measuring the thermal properties of materials. It has received significant attention in recent years due to its versatility, sensitivity, and the range of applications it can be used for. The main concept of FDTR is measuring the thermal response of a material and analyzing it as a function of frequency, rather than time. This frequency-based approach provides certain advantages, such as improved signal-to-noise ratio and the ability to capture a broader spectrum of thermal transport phenomena.

The principle of FDTR is founded on the phenomenon of thermoreflectance. When a material is subjected to a change in temperature, there is a corresponding alteration in its reflectivity. The change in reflectivity with respect to temperature is given by the coefficient of thermoreflectance, a property intrinsic to each material. This effect forms the basis of FDTR measurements, which

utilize a modulated pump beam to heat the sample and a probe beam to monitor the resulting temperature-dependent reflectivity changes.

The pump beam, modulated at a specific frequency, induces periodic temperature fluctuations within the sample. These fluctuations create thermal waves that propagate into the material. The depth to which these waves penetrate depends on the modulation frequency, with higher frequencies leading to more superficial penetration and lower frequencies resulting in deeper thermal wave propagation [32]. The penetration depth is formulated as [33]:

$$\ell = \sqrt{K/\pi C f}, \quad (2.1)$$

where  $K$  and  $C$  are the thermal conductivity and volumetric heat capacity of the material and  $f$  is the modulation frequency.

The reflected probe beam carries information about the thermal response of the sample. By analyzing the phase lag and amplitude reduction of the reflected probe signal relative to the modulation of the pump beam, information about the thermal properties of the sample can be extracted [27]. In analyzing the data, it is assumed that the sample's response to the laser beam is Linear Time Invariant (LTI). In order for this assumption to be true, the thermorefectance coefficient of the material should stay linear. This is only valid if the temperature rise in the sample is small, which for typical FDTR measurements, is usually the case [27]. Experimentally, this is ensured by checking whether the phase of the system stays consistent when increasing the pump laser power.

A significant advantage of FDTR is its sensitivity to various thermal transport regimes. By changing the modulation frequency of the pump beam, FDTR can access different heat transfer

regimes, from the diffusive to the ballistic [34], thereby providing a comprehensive picture of the thermal behavior of the material under investigation. If the frequency of the pump beam is low, the penetration depth will be high, and the heat conduction will be diffusive. As the frequency goes higher, the depth of penetration becomes shallower, at the point where it becomes smaller than the mean free path of the phonons in the sample,  $\ell_p < \text{MFP}$ , the conduction starts shifting from the diffusive regime into the ballistic area. Another benefit of FDTR is that it allows for the differentiation between in-plane and through-plane thermal properties by changing the amount of offset between the pump and probe beams, which is particularly beneficial when studying anisotropic materials or structures. This variation of FDTR called Beam Offset FDTR will be explored in detail in the next chapter.

In order to obtain accurate measurements, several aspects must be considered in FDTR experiments. First, some thermal properties of the sample and the coating layer used for the measurement need to be known or estimated. Moreover, the spatial profiles of the laser beams must be well-characterized. These parameters are then entered in multi-layer thermal models which are typically employed for data analysis in FDTR [26].

The versatility of FDTR allows it to be applied to a wide range of materials and structures, including metals, semiconductors, insulators, thin films, and more recently, two-dimensional materials. In all these cases, FDTR provides valuable insights into the thermal characteristics of these materials, thus contributing to their fundamental understanding and facilitating their application in areas such as electronics, photonics, and energy systems [35].

In addition to its standard configuration, several variants of FDTR have been developed to

address specific measurement challenges or to extend its capabilities. For instance, the beam-offset FDTR technique has been developed to measure the in-plane thermal conductivity of materials, with a higher sensitivity than regular FDTR [36]. Another variant of FDTR with improved sensitivity to lateral heat transport is Frequency Domain Magneto Optical Kerr Effect or FD-MOKE [37], in which a magnetic material is used as the transducer layer, utilizing the change in magnetization due to the temperature change as a means to investigate the samples.

In conclusion, Frequency Domain Thermoreflectance is a powerful tool for the investigation of thermal transport phenomena in a wide variety of materials. Its versatility makes it an indispensable technique in the field of thermal science.

## 2.2 Modeling

Analysis of frequency-domain thermoreflectance (FDTR) data involves the solution of the heat diffusion equation to model heat transfer and extract material's thermal properties from the phase and amplitude of the reflected probe beam. In its simplest form, the frequency domain solution for the surface temperature of a single layer material is given as follows [26]:

$$g(r) = \frac{e^{-qr}}{2\pi Kr} \quad (2.2)$$

$$q^2 = \frac{i\omega}{D} \quad (2.3)$$

$$D = \frac{K}{\rho c_p} \quad (2.4)$$

in which  $K$  is the thermal conductivity of the material,  $D$  is the thermal diffusivity,  $\omega$  is the angular frequency of the pump beam, and  $r$  the radial coordinate. In equation 2.4  $\rho$  is the density and  $c_p$  is the specific heat capacity, so that  $C = \rho c_p$ . Equation 2.2 describes how the temperature at the surface of a material can be calculated when it is being heated by a point heat source with the frequency  $\omega$ .

Since there is radial symmetry in this problem, Hankel transform can be used to simplify the convolution of this term later on with the laser beam intensity profiles since Hankel transform can be considered a two dimensional Fourier transform when there is circular symmetry. [26]:

$$G(h) = 2\pi \int_0^\infty g(r) J_0(2\pi hr) r dr \quad (2.5)$$

We get:

$$G(h) = \frac{1}{K(4\pi^2 h^2 + q^2)^{\frac{1}{2}}} \quad (2.6)$$

Where  $h$  is the Hankel transform variable and  $J_0(2\pi hr)$  is the zeroth order Bessel function of the first kind. To heat the surface of the sample the pump beam is used with a Gaussian intensity distribution of  $p(r)$  where the  $1/e^2$  radius of the pump beam is  $w_0$  [26]:

$$p(r) = \frac{2A}{\pi w_0^2} \exp\left(-2r^2/w_0^2\right) \quad (2.7)$$

for which the Hankel transform get calculated to be:

$$P(h) = A \exp\left(-\pi^2 h^2 w_0^2/2\right) \quad (2.8)$$

where  $A$  is the amplitude of the heat absorbed by the sample at frequency  $\omega$ . In order to calculate the surface temperature oscillations distribution  $\theta(r)$  for the sample the inverse transform of the



product of  $P(h)$  and  $G(h)$  can be taken:

$$\theta(r) = 2\pi \int_0^\infty P(h)G(h)J_0(2\pi hr)h dh \quad (2.9)$$

The data that is gathered through the probe beam is a weighted average of the temperature oscillations distribution  $\theta(r)$ :

$$\Delta\mathcal{T} = \frac{4}{w_1^2} \int_0^\infty \theta(r) \exp\left(-2r^2/w_1^2\right) r dr \quad (2.10)$$

In which  $w_1$  is the  $1/e^2$  radius of the probe beam. Taking this integral over  $r$  results in a Hankel transform which is then calculated numerically:

$$\Delta\mathcal{T} = 2\pi A \int_0^\infty G(h) \exp\left(-\pi^2 h^2 \left(w_0^2 + w_1^2\right)/2\right) h dh \quad (2.11)$$

This formula is for a single layer material. In order to solve this equation for a multi-layer sample, an algorithm developed by Feldman [38] is used which gives the solution for each layer iteratively based on the layer beneath. For the bottom layer, since heat is not able to reach the other side at a rate as fast as the modulation frequency,  $B^+ = 0$  and  $B^- = 1$  are taken for that layer.

$$\begin{pmatrix} B^+ \\ B^- \end{pmatrix}_n = \frac{1}{2\gamma_n} \begin{pmatrix} \exp(-u_n t_n) & 0 \\ 0 & \exp(u_n t_n) \end{pmatrix} \times \begin{pmatrix} \gamma_n + \gamma_{n+1} & \gamma_n - \gamma_{n+1} \\ \gamma_n - \gamma_{n+1} & \gamma_n + \gamma_{n+1} \end{pmatrix} \begin{pmatrix} B^+ \\ B^- \end{pmatrix}_{n+1} \quad (2.12)$$

$$u_n = \left(4\pi^2 h^2 + q_n^2\right)^{1/2} \quad (2.13)$$

$$q_n^2 = \frac{i\omega}{D_n} \quad (2.14)$$

$$\gamma_n = K_n u_n \quad (2.15)$$

The parameters in this equation are  $t_n$ ,  $D_n$  and  $K_n$  which are the thickness of the layer, thermal diffusivity and thermal conductivity of the corresponding layer with  $n$  being the number of the layer where  $n = 1$  is the top layer. To model the boundary conductance between the layers, each is modeled as a thin layer, usually around 1nm with a very low thermal conductivity. In order to combine equation 2.9 with Feldman algorithm,  $G(k)$  is taken as follows [26]:

$$G(h) = \left( \frac{B_1^+ + B_1^-}{B_1^- - B_1^+} \right) \frac{1}{\gamma_1}. \quad (2.16)$$

## 2.3 Ballistic vs. Diffusive Transport

As mentioned in the previous sections, FDTR can probe into heat transport regimes from diffusive to ballistic depending on various parameters such as spot size, modulation frequency and sample thickness. In the modeling it is assumed the heat transport is fully diffusive, since the criteria for staying in the diffusive regime have been met. In cases where the mean free path of the phonons becomes larger than the penetration depth of the beam or the thickness of the material or the spot size, non-diffusive transport can take place [33], which, if analyzed by a diffusive model, leads to thermal conductivities lower than the actual value since the contribution by the ballistic phonons has not been taken into account [34]. In general cases both the thickness of the materials and the spot sizes are in the range of micrometers whereas the phonon mean free paths are in the nanometer scale. As for the frequency of measurement, studies have observed reduced thermal conductivities due to the non-diffusive transport at frequencies up to 200MHz [33], however, most of the measurements

in this thesis are done at frequencies up to 20MHz.

## 2.4 Sensitivity

Sensitivity analysis is a crucial step in interpreting FDTR data and ensuring the accuracy of the thermal property measurements. The fundamental idea of sensitivity analysis is to understand how the phase of the signal changes when a parameter changes a specific percentage. In the measurements, the phase change of the signal for a change in parameter  $x$  is investigated and the formula is defined as [27,39]:

$$S = \frac{d\theta}{d \ln x} \quad (2.17)$$

where  $\theta$  is the phase of the measured signal and  $x$  is the parameter of interest. In the Matlab code a graph is plotted showing how much the signal phase will change if a parameter changes by 10%. This is done for all of the variables over the whole frequency range of measurement. In this way, one will know if the measurement is sensitive enough to the parameter that one is trying to fit for or if the measurement is taken in the correct frequency range where the signal is sensitive to the desired parameter.

When the sensitivity is calculated for each parameter and it is found that one parameter has a much larger phase change than the others, this indicates that the model is highly sensitive to that parameter. This sensitivity bears the information that the accuracy of the measurements is especially dependent on the accuracy of this particular parameter.

The sensitivity should also be compared to the typical noise of the measurement. If the sensitivity

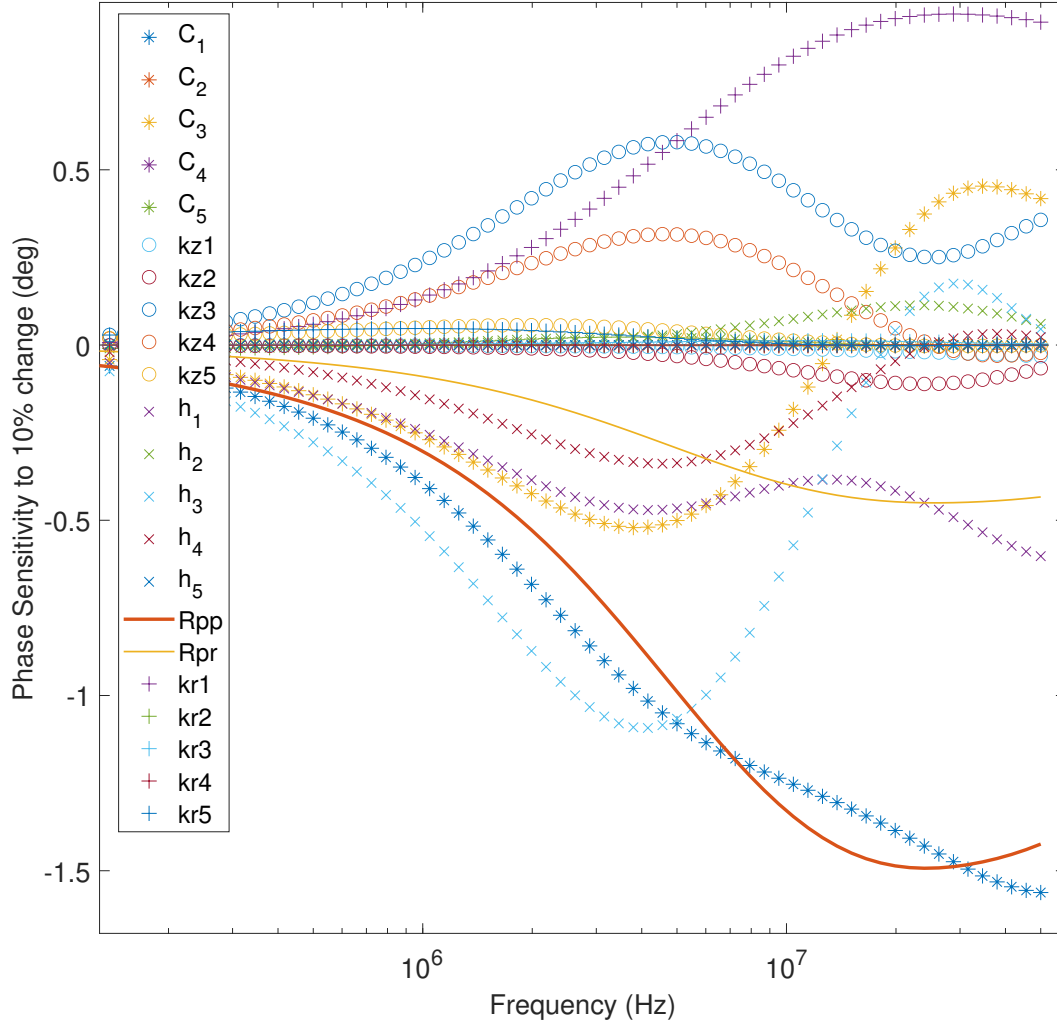


Figure 2.1: Thermal conductivity sensitivity analysis for Al/SiO<sub>2</sub>/Si sample. The spot sizes of pump and probe beams are 1.5 and 0.8  $\mu\text{m}$  respectively.  $kz$  and  $kr$  refer to the through-plane and in-plane thermal conductivities and the numbers represent the different layers of the sample.

to a parameter is below the noise, then it will not be possible to determine its value very accurately. The FDTR system used in this thesis typically has phase noise of 0.05 deg. So, for example, if the sensitivity to the thermal conductivity of the top layer of the sample is 0.1 deg for a 10% change in its value, this variation will be above the noise level of the measurement and its value can be expected to be determined within a 10% uncertainty.

Sample sensitivity analysis can be seen in Figure 2.1 for an Al/SiO<sub>2</sub>/Si sample with the even numbered layers being the boundaries between the materials. The thickness of the Al layer is around 50-60 nm and the SiO<sub>2</sub> layer is 150-160 nm. For example in this case, in order to be able to extract the thickness of the third layer, measurements should be done in frequency ranges between 1 and 10MHz since the model is sensitive to it in that frequency region. Another thing to note is that it might not be possible to get accurate results if it is attempted to extract the through-plane thermal conductivity of the first and fourth layer simultaneously since they have similar sensitivities with peaks almost in the same frequency, making it hard for the model to distinguish the phase change due to a increase or a decrease in one them. Finally, sensitivity analysis not only helps with identifying crucial parameters but also guides experimental design. By understanding which parameters the model is most sensitive to, the efforts can be focused on accurately measuring these parameters. As an example here it can be observed that the model is highly sensitive to properties of the first layer, so to get the most precise results, these parameters should be measured as accurately as possible and given to the model. Alternatively, if the model is insensitive to certain parameters, these parameters might be fixed at typical values rather than spend resources on their precise measurement. Thus, sensitivity analysis can enhance the efficiency and reliability of FDTR measurements.

## 2.5 Experimental Setup

The FDTR technique essentially operates using the principles of laser-induced heating and thermorefectance, which refers to the change in the reflectivity of a material with temperature [40]. The physical and optical aspects of FDTR can be comprehended by breaking down the setup into its key components.

**Laser Source and Modulation:** In Frequency Domain Thermorefectance (FDTR), a dual laser system named pump and probe technique is utilized. This laser system is divided into two parts, the pump laser and the probe laser. The pump laser is modulated at a frequency from kilohertz (kHz) to the megahertz (MHz) range with the help of a lock in amplifier. A DC bias brings the pump laser into linear operation mode and an AC signal varies the output power sinusoidally. Modulation of the pump beam is crucial as it creates a periodical temperature change in the sample surface which can then be observed by the probe beam.

**Optical System:** The optical system's function is to direct and focus the pump and probe beams onto the sample and back to the detector. In the setup used in this thesis, this system consists of a series of beam splitters, mirrors, and lenses. Beam splitters are used to direct the beams towards the sample, while mirrors are used to guide these beams along the optical path. An objective lens is used to focus the beams onto the sample surface.

**Thermal Oscillations and Reflectivity Change:** As the modulated pump beam shines on the sample, it causes periodical thermal oscillations. These oscillations create a change in the sample's temperature, which in turn influences the sample's reflectivity. This change in reflectivity affects the intensity of the reflected probe beam. Hence, the probe beam essentially carries the thermal

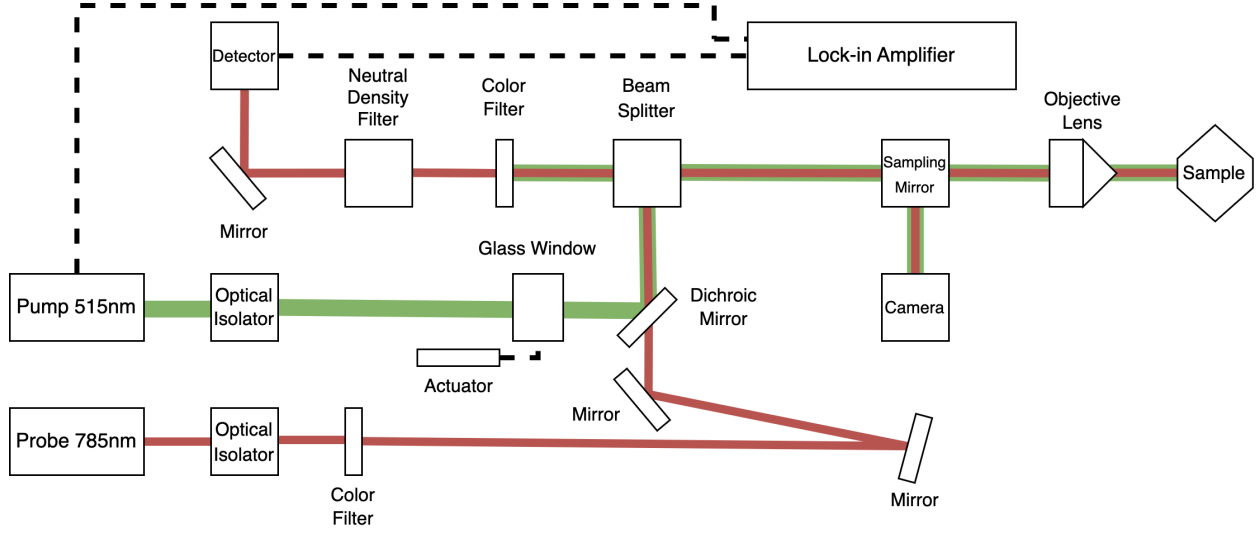


Figure 2.2: Detailed representation of the FDTR Setup

response of the sample to the modulated heating. This thermal response can then be analyzed to determine the sample's thermal conductivity.

**Signal Detection:** The thermorefectance signal captured by the probe beam is collected and measured using a photodetector. The photodetector translates the changes in light intensity into an electrical signal. To accurately interpret this signal, a lock-in amplifier is used. This device is synchronized with the frequency of the pump modulation and is able to extract the relevant data from the thermorefectance signal [27]. The lock-in amplifier provides the amplitude and phase components of the signal. These components contain important information about the thermal characteristics of the material being studied, such as thermal conductivity and heat capacity.

An overall diagram of the whole FDTR setup as used in this thesis can be seen in Figure 2.3. The optical isolators pass the beam only in one direction, preventing any beam to shine back at the laser sources and destabilize them. Similarly, the color filter in front of the probe laser prevents any

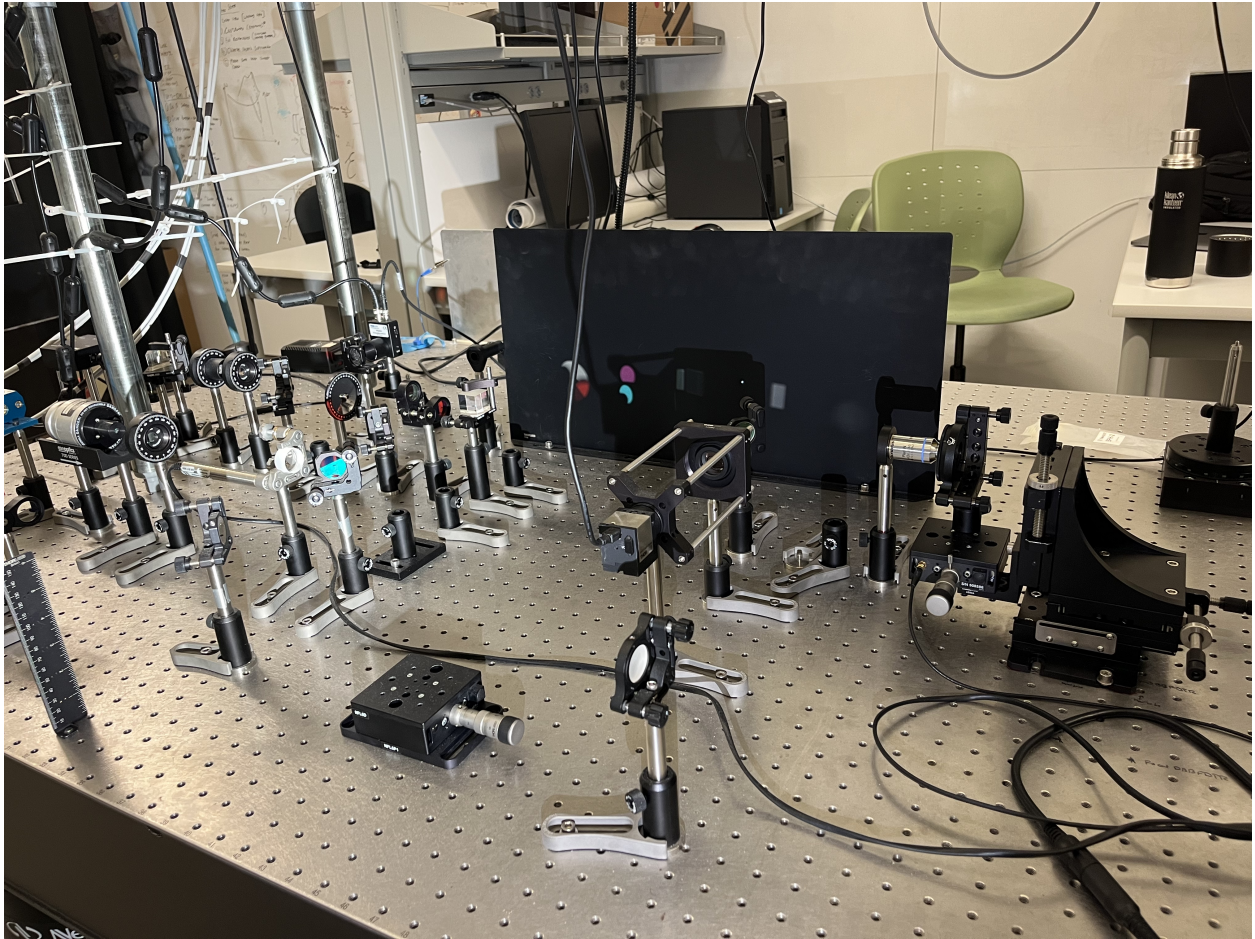


Figure 2.3: The FDTR Setup

parasitic back reflections of the pump beam from entering the probe laser source and causing noise in the measurements. The role of the neutral density filter is to adjust the amount of light entering the detector to prevent flooding the sensor. The color filter before the detector makes it possible to choose between making measurements of the thermorefectance, by blocking the pump beam, or measuring the reference phase of the system (more on this later), by blocking the probe beam.



## 2.6 Spot Size

In Frequency Domain Thermoreflectance (FDTR) measurements, the laser spot size is a crucial parameter as it determines the spatial resolution of the experiment and affects the heat diffusion process. The spot size refers to the  $1/e^2$  radius of the laser beam that interacts with the material surface.

**Spatial Resolution:** The spatial resolution of FDTR is approximately equivalent to the spot size of the laser [41]. In experiments where the thermal properties of the material vary across the surface (e.g., in composite materials or at interfaces), having a small spot size allows for more precise local measurements of thermal conductivity. The spatial resolution is also affected by the thermal penetration of the thermal waves at a given frequency, so the resolution is dominated by the optical spot size if the thermal waves diffuse over distances smaller than the spot size.

**Heat Diffusion:** The heat generated by the pump laser beam diffuses radially outward from the point of laser-material interaction. The extent of this diffusion is a function of the thermal diffusivity of the material, the modulation frequency of the pump beam, and the laser spot size in the form of the following equations [42]:

$$\ell_r = \sqrt{K_r / \pi C f}, \quad (2.18)$$

$$\ell_r \ll \frac{1}{4} \sqrt{r_{pp}} \quad (2.19)$$

$$r_{pp} = r_{pump}^2 + r_{probe}^2 \quad (2.20)$$

When the length of the radial diffusion is sufficiently smaller than the spot sizes according to the above equations, radial transfer of heat can be neglected.

Ballistic and Diffusive Heat Transfer: The spot size and modulation frequency can control the regime of heat transfer (ballistic or diffusive) [34] as described earlier in section 2.3. For a small spot size and high frequency, the heat has less time to diffuse, leading to ballistic heat transfer. On the other hand, a larger spot size and lower frequency allow for more heat diffusion, making the heat transport diffusive.

Therefore, determining and maintaining the appropriate laser spot size is a critical aspect of FDTR measurements. It directly impacts the resolution, accuracy, and interpretation of the data. Therefore, careful consideration must be given to select the optimal spot size, depending on the specific requirements of the experiment. The spot size is measured using a method named razor profiling. In this method the setup is first prepared for a normal FDTR measurement but with a laser power meter on the way of the reflected beam instead of the photodetector. With the beam focused on the edge of the sample, a piezo stage shifts the sample a few micrometers out of the beam area so that no light reaches the power meter. Then it will gradually bring back the sample into the light field, creating a Gaussian beam profile on the power meter which can then be analyzed to extract the spot size. This procedure is repeated for both the pump and probe beams. Samples of razor profiling graphs and their Gaussian fits can be observed in Figures 2.4 and 2.5.

## **2.7 Matlab Code**

The measured data is analyzed using a code written in Matlab. The formulas discussed in 2.2 are utilized in the code to fit the data to the model and calculate the desired parameters. It is mainly based on the work done by Feser's group [43] which is written for TDTR. The code is adopted

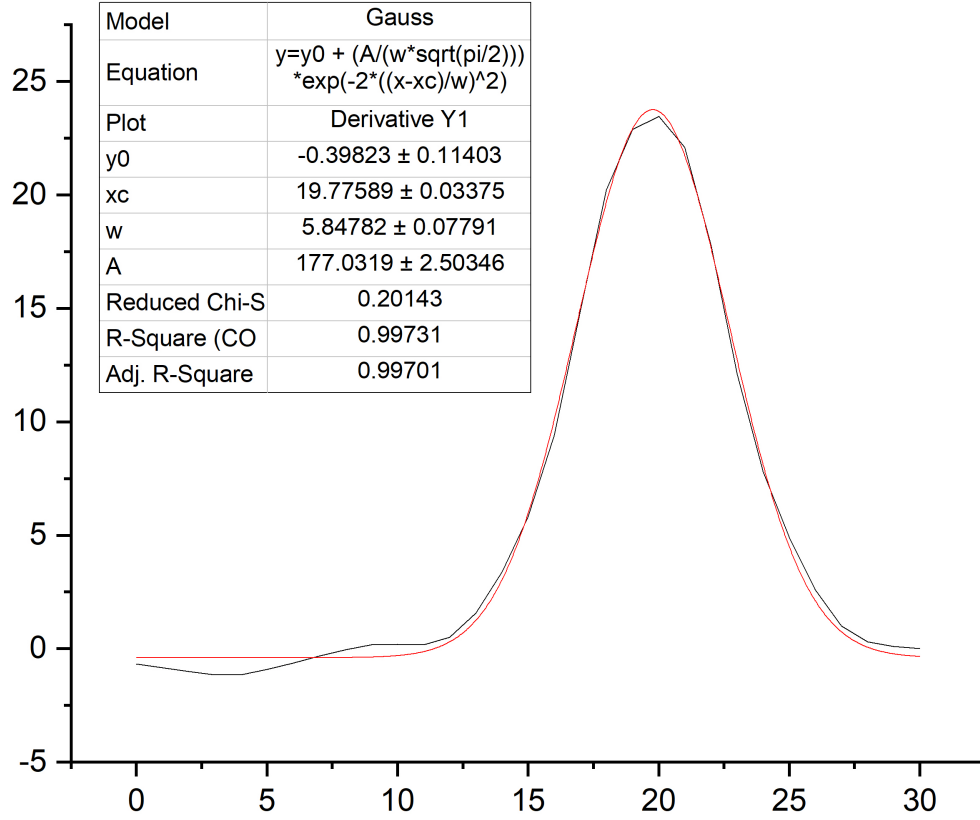


Figure 2.4: Razor profiling analysis for the pump laser. W in the parameters list is the radius of the beam in micrometers. The horizontal axis is the movement of the sample in micrometers and the vertical axis is the derivative of the laser intensity from the power meter.

accordingly to work with FDTR systems. The input data for the code is the signal's phase and amplitude from each measurement point calculated by subtracting the reference measurement data from the normal measurement. The point of doing two subsequent measurements, one with the detector receiving the probe beam (the normal measurement) and one with the pump beam reaching the detector (the reference measurement) is to eliminate any inherent optical and electronic delays in the system causing phase changes in the data.

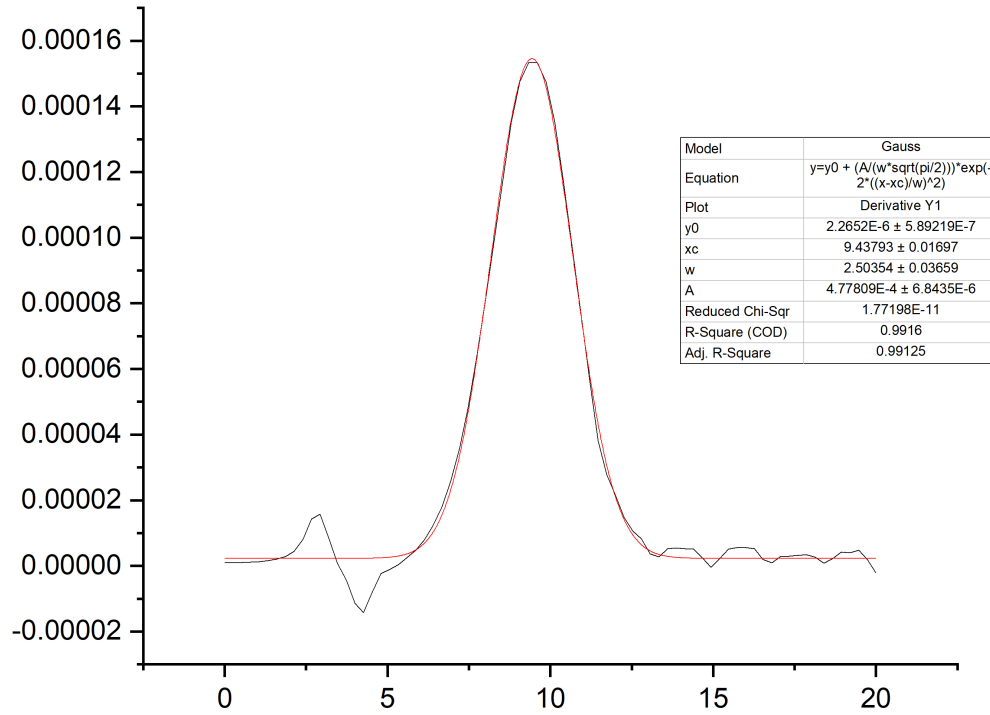


Figure 2.5: Razor profiling analysis for the probe laser. W in the parameters list is the radius of the beam in micrometers. The horizontal axis is the movement of the sample in micrometers and the vertical axis is the derivative of the laser intensity from the power meter.

The parameters of each layer are entered in the code as matrices and the unknown parameters are selected to be fitted for as in Figure 2.6b. The output of the code will be a graph showing the quality of the fit depicting the answer that the code came up with for each measurement point compared to the actual data measured for that point. An example of this is shown in Figure 2.6c. At the end of the program the fitted values for the desired parameters will be printed out, along with their standard errors which are calculated from the Jacobian matrix, and a metric that expresses whether any of the parameters being fitted are interdependent. In the case of a sample composed of a gold layer on Kapton tape, these can be seen in Figure 2.6a.

## 2.8 Summary

Frequency Domain Thermorefectance (FDTR) is a powerful and non-invasive method for measuring the thermal conductivity of a wide range of materials, from bulk to few layers. This technique operates based on the thermorefectance principle, where the temperature-induced changes in the reflectivity of a material are monitored. FDTR employs two laser beams: a pump beam that periodically heats the material, and a probe beam that detects the resulting temperature-dependent reflectivity changes.

This non-contact method relies on a complex interplay of optical and thermal phenomena. The pump beam generates a sinusoidally varying heat source on the sample, which causes a temperature oscillation on the material surface. This temperature oscillation induces a reflectivity change, which is sensed by the probe beam. The phase lag and amplitude of the reflected probe beam yield crucial information about the thermal properties of the material under test.

The mathematical modeling of the FDTR measurement process requires an understanding of heat transfer theory and the specific characteristics of the material. The heat equation, which governs the heat diffusion process, is solved in the frequency domain. This requires considering several parameters, including the thermal conductivity, heat capacity, layer thicknesses, and the thermal boundary conductance. The theoretical model is then used to fit the experimental data, allowing the extraction of the material's thermal properties.

Sensitivity analysis plays a significant role in this fitting process. It assesses how changes in input parameters (such as thermal conductivity, heat capacity, etc.) affect the output or model predictions. This is commonly conducted using derivatives to understand how a slight variation in a

parameter influences the modeled FDTR signal. The outcome of a sensitivity analysis guides the choice of modulation frequency in experiments and helps identify the thermal parameters that can be determined accurately from the FDTR measurements.

The physical and optical setup for FDTR experiments necessitates careful design and calibration. The laser spot size is a critical parameter, affecting spatial resolution, heat diffusion, thermal boundary conductance measurement, pump-probe overlap, and the regime of heat transfer (ballistic or diffusive). Thus, the appropriate selection of the laser spot size, depending on the specific experimental needs, is essential.

In summary, FDTR is a sophisticated, non-destructive method for characterizing thermal properties of materials. It combines advanced optics, intricate mathematical modeling, sensitivity analysis, and carefully designed experimental setups to deliver accurate thermal conductivity measurements. This technique holds promise for diverse fields, such as materials science, microelectronics, and nanotechnology, where understanding and manipulating heat flow are of paramount importance.

```

ans =
    5.159173000494405e-08
se =
    3.289661965410167e-09
lambda=[310 0.12]; %W/m-K
C=[2.49 1.54]*1e6; %J/m^3-K
t=[50 125000]*1e-9; %m
lambda_r=[58.5 0.12];%kr
r_pump=1.5e-6; %pump 1/e^2 radius, m
r_probe=0.8e-6; %probe 1/e^2 radius, m

```

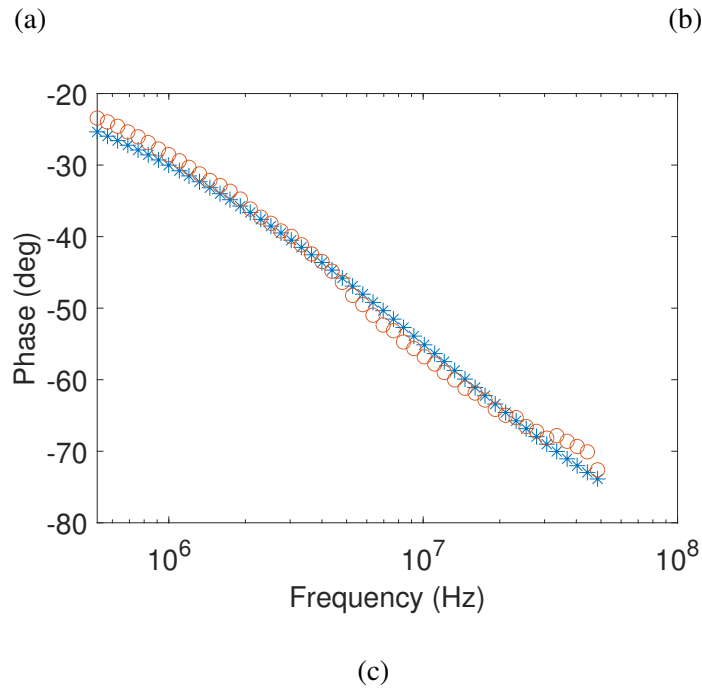


Figure 2.6: Sample fit for the thickness of gold layer on Kapton tape. (a) Fitted thickness and standard error, in meters, (b) Parameter matrix for the 2-layered sample where  $\lambda$  and  $\lambda_r$  are the through- and in-plane thermal conductivity, and  $C$  and  $t$  are the volumetric heat capacity and thickness. (c) A plot comparing the measured thermal phase versus frequency (red circles) with the model for the best fit (blue stars).

# **Chapter 3**

## **Beam Offset Frequency Domain**

## **Thermoreflectance**

### **3.1 Overview**

Beam-offset Frequency Domain Thermoreflectance (BO-FDTR) [36] is a variation of the traditional Frequency Domain Thermoreflectance (FDTR) method. Like its parent method, BO-FDTR employs a pump-probe system to induce and then detect temperature oscillations in a sample. However, in BO-FDTR, the pump and probe beams are deliberately misaligned or offset by a specific amount to enhance the sensitivity of the setup to in-plane thermal properties of the material under test.

The mathematical modeling for BO-FDTR analysis is a bit more complex than the conventional FDTR since the pump and probe beams are no longer concentric in this arrangement. The model should also take into account parameters such as the amount of the beam offset and any ellipticity



in the spot size. In terms of sensitivity, the BO-FDTR method offers unique advantages due to the ability to distinguish different directions of heat conduction in the sample. As visible in Figures 3.1 and 3.2, by adding an offset amount of  $2\text{ }\mu\text{m}$  between the pump and probe beams, the sensitivity peaks relating to different in-plane and out-of-plane conductivities of each layer become separated and more distinguishable from each other, making it possible to fit for these parameters. The possibility of varying the beam offset enables the tuning of sensitivity towards different thermal properties. Smaller offsets can emphasize the vertical heat transport, while larger offsets can highlight the in-plane heat transport. This makes BO-FDTR a highly versatile tool for thermal characterization, allowing for tailored measurements depending on the specific material or application in question.

In conclusion, BO-FDTR represents a powerful advancement in non-invasive thermal measurement techniques, offering enhanced sensitivity and specificity towards in-plane thermal properties and providing unique insights into anisotropic heat transfer behavior. Its ability to discern different heat transfer pathways can be crucial in fields like materials science, nanotechnology, and electronics, where the directionality of heat transport is of paramount importance.

## 3.2 Theory

BO-FDTR operates on the principles similar to normal FDTR but has different calculations methods due to the beams not being concentric.

To understand BO-FDTR, first the equation for the temperature fluctuation due to the pump beam which is detected by the probe beam, given by [44] needs to be considered

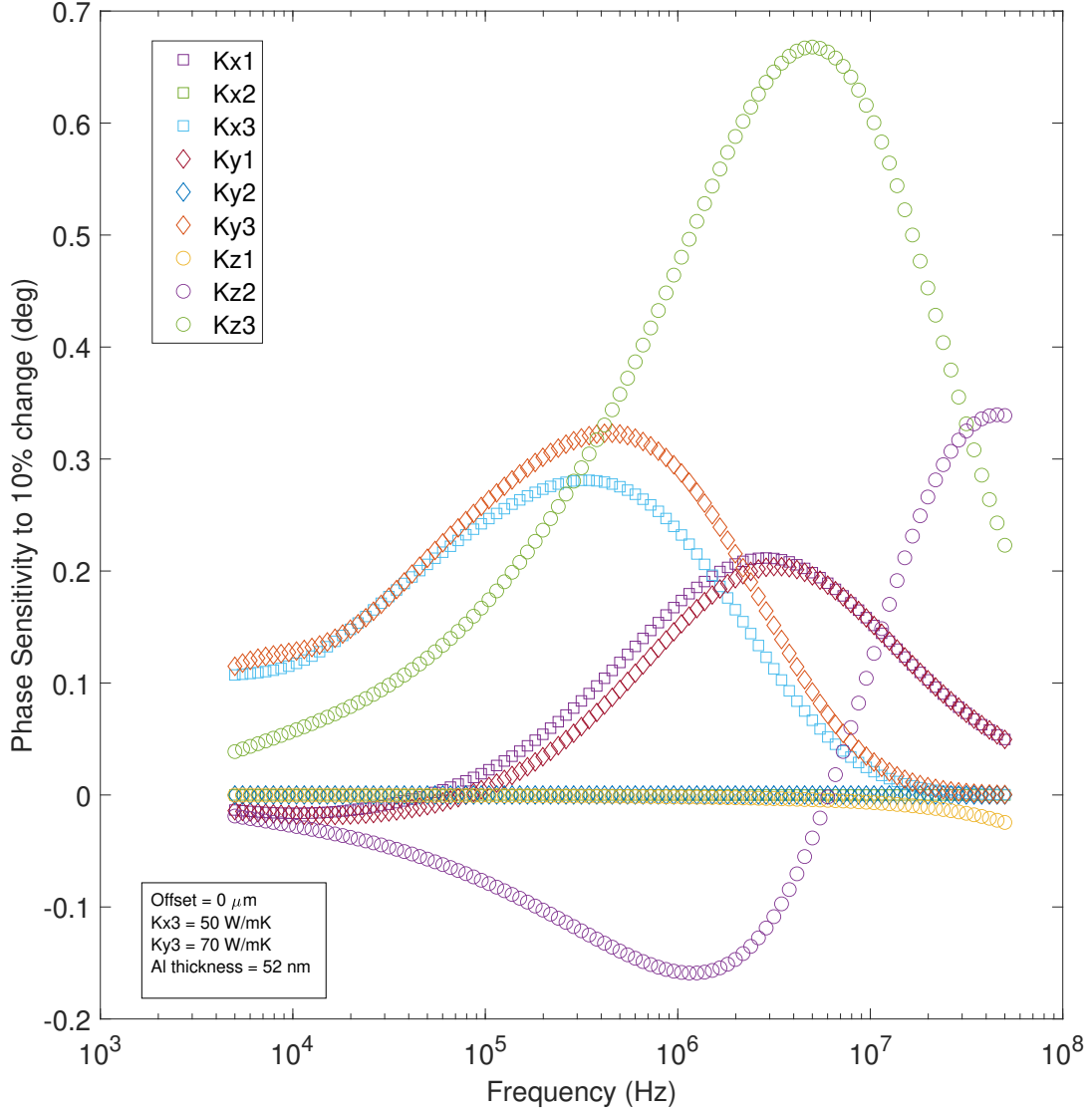


Figure 3.1: Sample sensitivity analysis with no offset for Al/ReS<sub>2</sub>. The spot sizes of pump and probe beams are 5.8 and 2.5  $\mu\text{m}$  respectively. Kx, Ky, and Kz refer to the three directions of thermal conductivity and the numbers represent the different layers of the sample. Sensitivities of Kx3 and Ky3 have very similar peaks making them indistinguishable to fit for simultaneously.

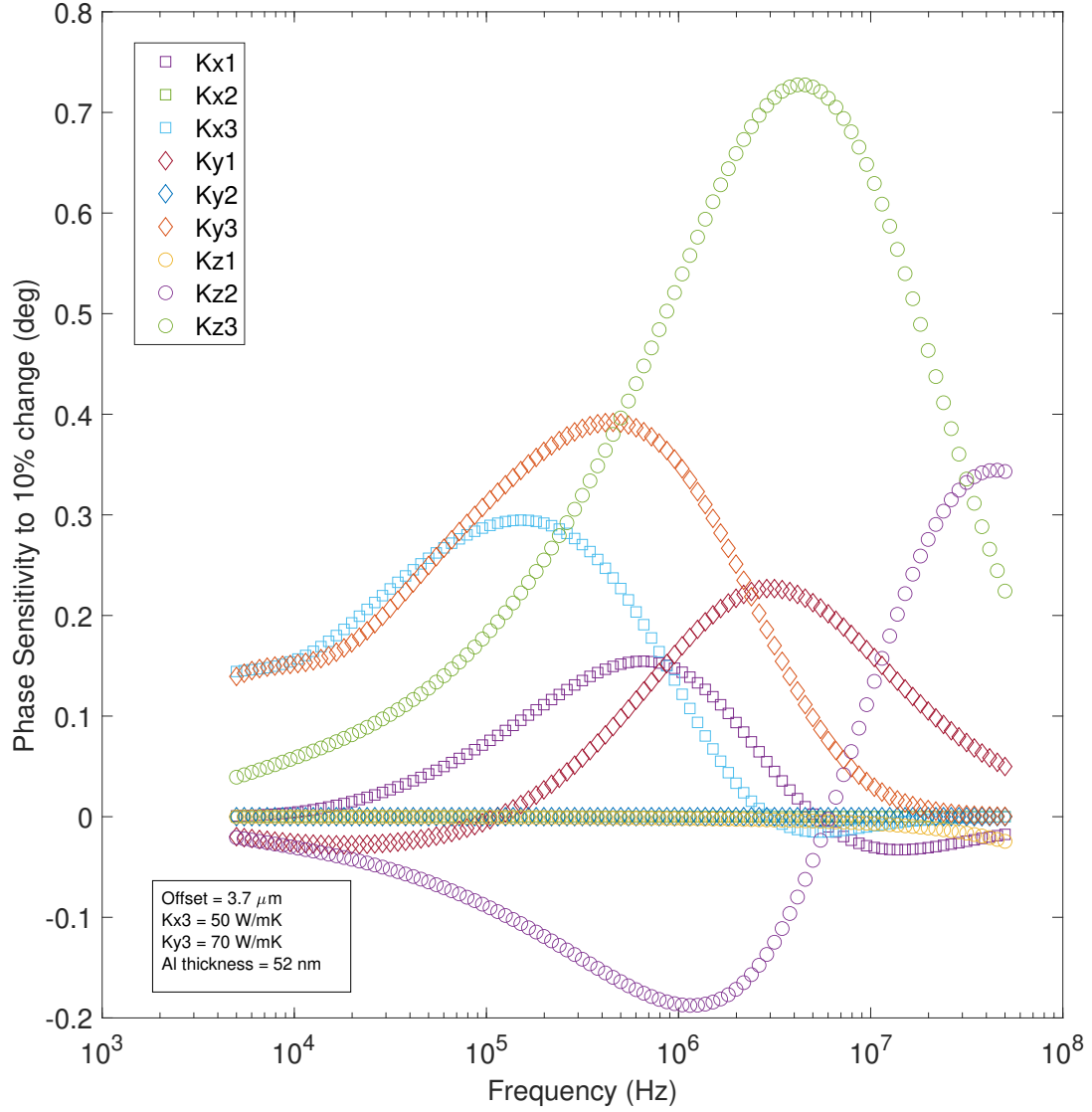


Figure 3.2: Sample sensitivity analysis for Al/ReS<sub>2</sub> with 3.7  $\mu\text{m}$  offset. The spot sizes of pump and probe beams are 5.8 and 2.5  $\mu\text{m}$  respectively. Kx, Ky, and Kz refer to the three directions of thermal conductivity and the numbers represent the different layers of the sample. The offset separates Kx3 and Ky3 peaks making them distinguishable from each other making it possible to fit for them simultaneously.

$$\Delta T(f) = \frac{2\pi}{A_S} \int_0^\infty G(f, h) P(h) S(h) h dh \quad (3.1)$$

where  $A_S$  is the total intensity of the probe beam, and  $P(h)$  and  $S(h)$  are the Hankel transforms of the pump and probe beams intensity profiles with  $h$  being the Hankel transform variable. In the case of an offset beam by an  $x_0$  amount,  $S(h)$  gets defined as [44]:

$$S(h) = \frac{A_S}{\pi} \exp\left(-\left[\left(\frac{\sqrt{2}x_0}{w_S}\right)^2 + \left(\frac{\pi w_S h}{\sqrt{2}}\right)^2\right]\right) \times \sum_{n=0}^{\infty} \frac{1}{(n!)^2} \left(\frac{\sqrt{2}x_0}{w_S}\right)^{2n} \ell_n\left(\frac{w_S h}{\sqrt{2}}\right). \quad (3.2)$$

$\ell_n(x)$  is defined recursively as [44]:

$$\ell_{n+1}(x) = -\frac{1}{x} \left[ \left( \pi^2 x^3 - x \right) \ell_n(x) + \left( \frac{1}{4\pi^2} - x^2 \right) \ell'_n(x) + \frac{x}{4\pi^2} \ell''_n(x) \right] \quad (3.3)$$

where  $\ell_0 = \pi$  is used for the first polynomial.

As already described in the previous chapter,  $G(f, h)$  is calculated using the Feldman algorithm:

$$G(f, h) = \left( \frac{B_1^+ + B_1^-}{B_1^+ - B_1^-} \right) \frac{1}{\gamma_1} \quad (3.4)$$

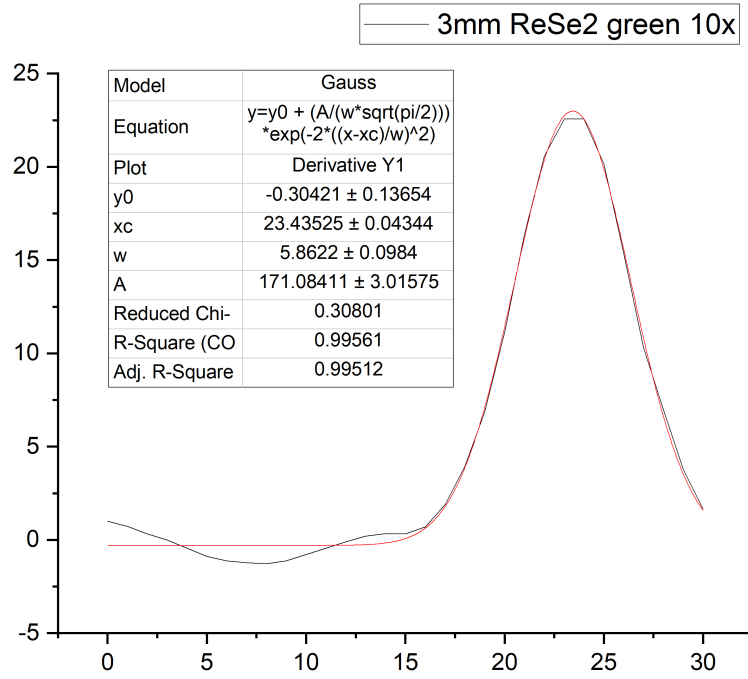
In the case of anisotropic materials we have [44]:

$$\gamma_n \equiv K_{z,n} u_n \quad (3.5)$$

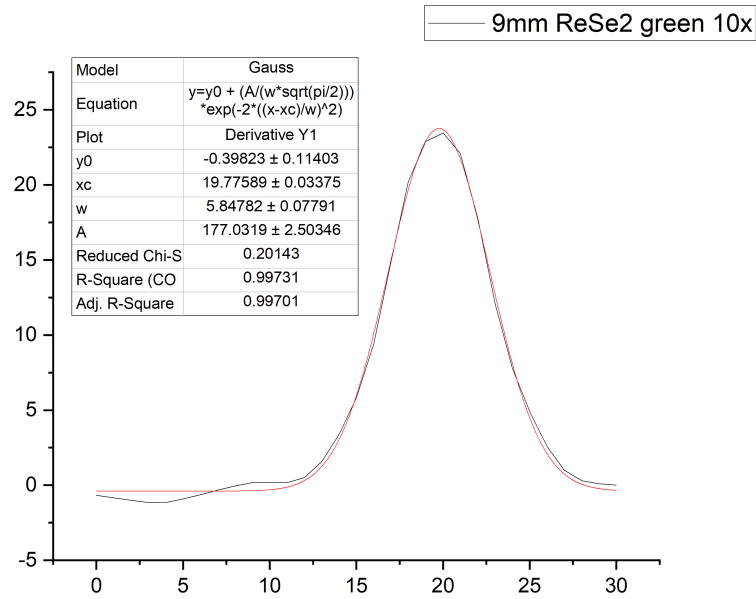
$$u_n \equiv \left[ 4\pi^2 h^2 \left( \frac{K_r}{K_z} \right) + q_n^2 \right]^{1/2} \quad (3.6)$$

with  $K_z$  and  $K_r$  being the through-plane and in-plane components of the thermal conductivity of each layer.





(a)



(b)

Figure 3.4: Calculating beam offset using razor profiling method

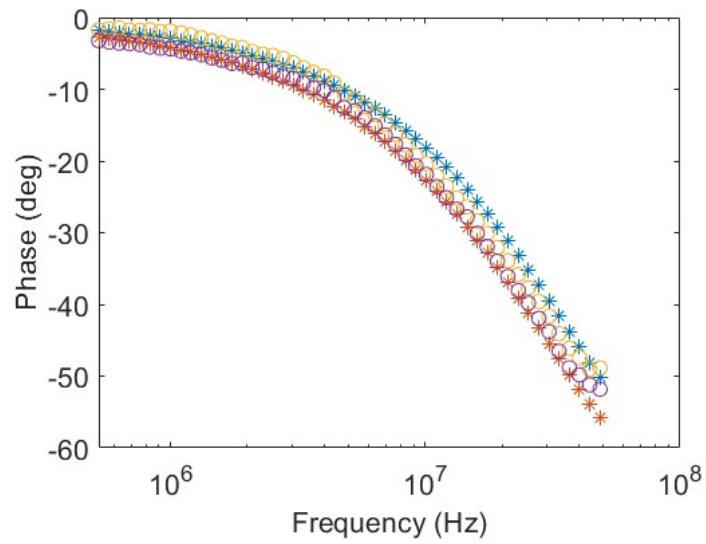
razor profiling method described in the previous chapter. Two subsequent razor profiles are acquired and by subtracting the centers of the Gaussian beams calculated from the fits, the amount of the offset can be determined. The razor profiles for the pump beam with the actuator being at 3mm and 9mm positions are shown in Figure 3.4. The xc parameter in the list is the center of the beam profile. By subtracting the two centers from each other the  $3.7 \mu\text{m}$  offset is obtained which was used in the measurements.

As an example of the BO-FDTR setup's capabilities, a sample of anisotropic graphite has been analyzed. The results for both in-plane and through-plane thermal conductivities, as well as the quality of the fits for concentric and offset positions, are presented in Figure 3.5. The through-plane thermal conductivity was found to be  $6.9 \text{ W/mK}$ , in contrast to the in-plane thermal conductivity, which was measured at  $869 \text{ W/mK}$ . This study utilized an approach where data from multiple measurements with varying offsets (including no offset and  $1.1 \mu\text{m}$  offset) were combined for enhanced accuracy. The observed in-plane thermal conductivity of this graphite sample is notably lower than the typical value of up to  $2000 \text{ W/mK}$  often reported for Highly Ordered Pyrolytic Graphite (HOPG). This discrepancy can be attributed to several factors specific to this measured sample. Firstly, the graphite flakes in this sample likely exhibit a lower degree of order compared to HOPG. Secondly, the lateral dimensions of the flake are not significantly larger than the laser spot size used in the measurements, potentially leading to non-diffusive transport effects that can lower the apparent thermal conductivity. These factors collectively contribute to the observed reduction in in-plane thermal conductivity, demonstrating the sensitivity and utility of the BO-FDTR technique in capturing variations in thermal conductivity due to structural differences in materials.

```
ans =
    6.921906021033922e+00    8.691238782490652e+02

se =
    1.563436955260637e+00    1.875065748361647e+02
```

(a)



(b)

Figure 3.5: Measuring thermal conductivity of graphite using BO-FDTR



In summary, the BO-FDTR system is a variation of normal FDTR with enhanced sensitivity to in-plane thermal conductivity, making it an invaluable tool in thermal materials research.

## Chapter 4

# Anisotropic Thermal Conductivity

## Measurement in Rhenium Dichalcogenides<sup>1</sup>

Frequency Domain Thermorefectance (FDTR) is an experimental technique extensively used to measure thermal properties, especially thermal conductivity, of various materials [27, 40, 41, 45, 46]. This non-destructive, optically-based method primarily involves inducing and monitoring temperature oscillations within the material under study, providing insights into its thermal response [26]. The FDTR implementation used in this study has been detailed elsewhere [36] as well as in chapters 2 and 3. Briefly, the setup operates on a 515 nm pump and a 785 nm probe laser. The laser beams are focused onto the sample using a 10× objective, resulting in a spot size of 5.8  $\mu\text{m}$  for the pump and 2.5  $\mu\text{m}$  for the probe beam measured using razor profiling. The pump beam is modulated from a few kHz up to tens of MHz to span frequencies with the highest sensitivity to the thermal conductivity of

---

<sup>1</sup>Parts of this thesis have been published in S. Tahbaz and S. Pisana, "Extreme in-plane thermal conductivity anisotropy in Rhenium-based dichalcogenides", Journal of Physics: Materials, under review

the samples. Two different measurements are made in order to recover the thermal phase response of the sample. A first measurement gathers data from the sample, and a subsequent reference measurement allows us to account for the phase shifts in the data due to the optical path of the laser beams and the electronics. The thermal phase response of the sample obtained by subtracting these two measurements is then fitted to the model to obtain the desired thermal properties of the sample.

While conventional FDTR provides valuable data on the thermal properties of the material and can distinguish in-plane from through-plane transport, it does not differentiate the thermal characteristics along different in-plane directions. To overcome this limitation, beam-offset FDTR (BO-FDTR) [36,44] is employed. In BO-FDTR [47], a spatial offset is introduced between the pump and the probe beam, making the measurement more sensitive to the thermal conductivity in the direction of the offset. This configuration allows sampling the thermal waves that propagate laterally across the material, effectively enabling the extraction of direction-dependent thermal properties. The BO-FDTR technique thus offers a more nuanced investigation of in-plane anisotropy, making it particularly suitable for studying materials like  $\text{ReS}_2$  and  $\text{ReSe}_2$  where this anisotropy is quite large. In order to create the offset between the two beams in the setup, the pump beam passes through a thick glass window mounted on a linear actuator, resulting in a  $3.7 \mu\text{m}$  beam offset on the sample surface for a 9 mm actuator displacement.

## **4.1 Modeling FDTR Data**

The method used to extract the thermophysical parameters of interest from FDTR is well documented in the literature [26,42]. It involves using the frequency-domain solution of Fourier's Law in

cylindrical coordinated in layered media, and weighting the response according to the pump and probe beams' Gaussian shape. Generally, the sample's thermal response is modeled by specifying thermal conductivity ( $K$ ), thickness ( $t$ ) and volumetric heat capacity ( $C$ ) for each layer, and thermal boundary conductance ( $G$ ) of each interface. All parameters are assumed to be known except for the unknowns of interest. In the present study, a solution is implemented that takes into account for beam offsets in anisotropic media initially developed by Feser and Cahill [48], which is generalized  $K$  to be a  $3 \times 3$  tensor. The tensorial representation, together with beam-offsetting, makes it possible to resolve  $K$  in distinct directions both within the plane of the sample (in-plane) and perpendicular to it (through-plane). It should be noted that a  $3 \times 3$   $K$ -tensor for a triclinic crystal has no zero elements, and due to Onsager's Theorem the tensor is symmetric, leading to a tensor of the form

$$\begin{bmatrix} K_{xx} & K_{xy} & K_{xz} \\ K_{xy} & K_{yy} & K_{yz} \\ K_{xz} & K_{yz} & K_{zz} \end{bmatrix} \quad (4.1)$$

where the indices are defined according to  $q_i = -K_{ij} \frac{\partial T}{\partial x_j}$ ,  $q$  is the heat flux along  $i$  giving rise to a temperature ( $T$ ) gradient along  $j$ . Equation 4.1 specifies three spatially orthogonal values for  $K$  and three angles with respect to the coordinate system of the FDTR experiment. It is not possible to simultaneously solve for all these unknowns in the experiment. However, the approximation is made that the  $c$ -axis is perpendicular to the plane of the substrate on which the crystal is placed and that the  $a$  and  $b$  axes are nearly orthogonal to the  $c$ -axis. These approximations are supported by the fact that layered crystals like TMDs cleave more easily across the  $c$ -axis and the unit cell angles with respect to the  $c$ -axis are  $88^\circ$  and  $75^\circ$  for  $\text{ReS}_2$  and  $92^\circ$  and  $104^\circ$  for  $\text{ReSe}_2$ . This implies that

within this approximation the orientation of the crystal can be taken to have the  $c$ -axis perpendicular to the substrate, and approximate  $K_{xz} \approx K_{yz} \approx 0$ . Proceeding this way, the remaining unknowns are  $K_{xx}$ ,  $K_{yy}$ ,  $K_{zz}$  and the angle of the basal plane of the crystal with respect to the FDTR offset direction that gives rise to  $K_{xy}$ . The basal plane orientation is uniquely identified by polarized Raman spectroscopy. For simplicity, in the rest of this chapter  $K_z$  will be referred to as the through-plane thermal conductivity and it is taken to be along the  $c$ -axis, and  $K_r(\theta)$  represents the angle-dependent thermal conductivity along the basal plane of the crystal.

Measurements of the thermal phase of the sample are taken as a function of modulation frequency for a fixed pump-probe offset, and the offset direction is changed with respect to a sample's crystal orientation by rotating the sample. For each offset direction,  $K_x$  (the in-plane conductivity in the direction of the beam offset),  $K_y$  (the in-plane conductivity in the direction perpendicular to the beam offset) and  $K_z$  (the through-plane conductivity) are fitted for. Then  $K_r(\theta) = [K_x(\theta) + K_y(\theta + 90^\circ)]/2$ . This makes it possible to take the average of equivalent results of the fits. All other thermophysical parameters are taken as known. Namely, the transducer thin film properties are determined on areas of the substrate without the crystal, together with the substrate properties, as explained below. The full list of parameters used in the model, sample FDTR data with corresponding model fits, reference measurements to obtain parameters that were held constant are given in the following sections, together with sensitivity analysis of the measurements to the parameters of interest and fitted parameter dependency.

## 4.2 Sample Preparation and Characterization

Samples of  $\text{ReSe}_2$  and  $\text{ReS}_2$ , were prepared via slightly different methodologies, although either approach yields equivalent results. Bulk crystals were procured from 2D Semiconductors.

The preparation of the  $\text{ReSe}_2$  flakes was done by mechanical exfoliation [49], a popular technique employed in the preparation of 2D materials [50, 51]. After exfoliation, the flake was transferred to Kapton tape, which was firmly secured with double-sided tape on a glass slide. Subsequently, this assembly was coated with a layer of  $\sim 50$  nm Al via electron-beam deposition.

The  $\text{ReS}_2$  crystal was also mechanically exfoliated. However, instead of transferring the exfoliated flakes to a Kapton tape support, they were transferred to a 300 nm  $\text{SiO}_2$  / Si substrate. The transfer of flakes onto this substrate was accomplished through the use of thermal release tape [52, 53] at a temperature of  $105^\circ$  C. This method was utilized to obtain larger flake sizes. Following the transfer, the flakes were coated with a  $\sim 50$  nm layer of Al by sputter deposition.

The thickness of the flakes were determined using a Bruker optical profilometer. The flakes had a thickness of  $\sim 3$   $\mu\text{m}$  for the  $\text{ReS}_2$  and  $\sim 10$   $\mu\text{m}$  for  $\text{ReSe}_2$  as evident in Figures 4.1b and 4.2b, respectively. The flakes are thus thick enough that entirely diffusive transport is expected at room temperature, since a thickness dependence of  $K$  would arise when the thickness is of the order of the phonon mean free paths. No dependence was detected in  $\text{ReS}_2$ , for example, down to a thickness of 60 nm [9]. Furthermore, the diffusive thermal wave penetration in the through-plane direction is given by  $\sqrt{K_z/\pi C_v f}$  and estimated to be within  $\sim 1.7$   $\mu\text{m}$  for  $\text{ReS}_2$  and  $\sim 8$   $\mu\text{m}$  for  $\text{ReSe}_2$ . Therefore, even for the lowest modulation frequencies used in the FDTR measurements (35 kHz for  $\text{ReS}_2$  and 5 kHz for  $\text{ReSe}_2$ ), the presence of the bottom crystal boundary would not be detected. This is

supported by the fact that the FDTR model fits are independent of the presence of the substrate in the model, thus the crystals can be taken as being semi-infinite.

Polarized Raman spectra [54] were collected with a Renishaw inVia Reflex at 532 nm for each of the flakes prior to deposition of the Al layer. The flakes were rotated in 15° steps relative to the polarization of the Raman beam [55] and the intensity of the prominent peaks for each material were recorded, allowing for the identification of the crystal axes.

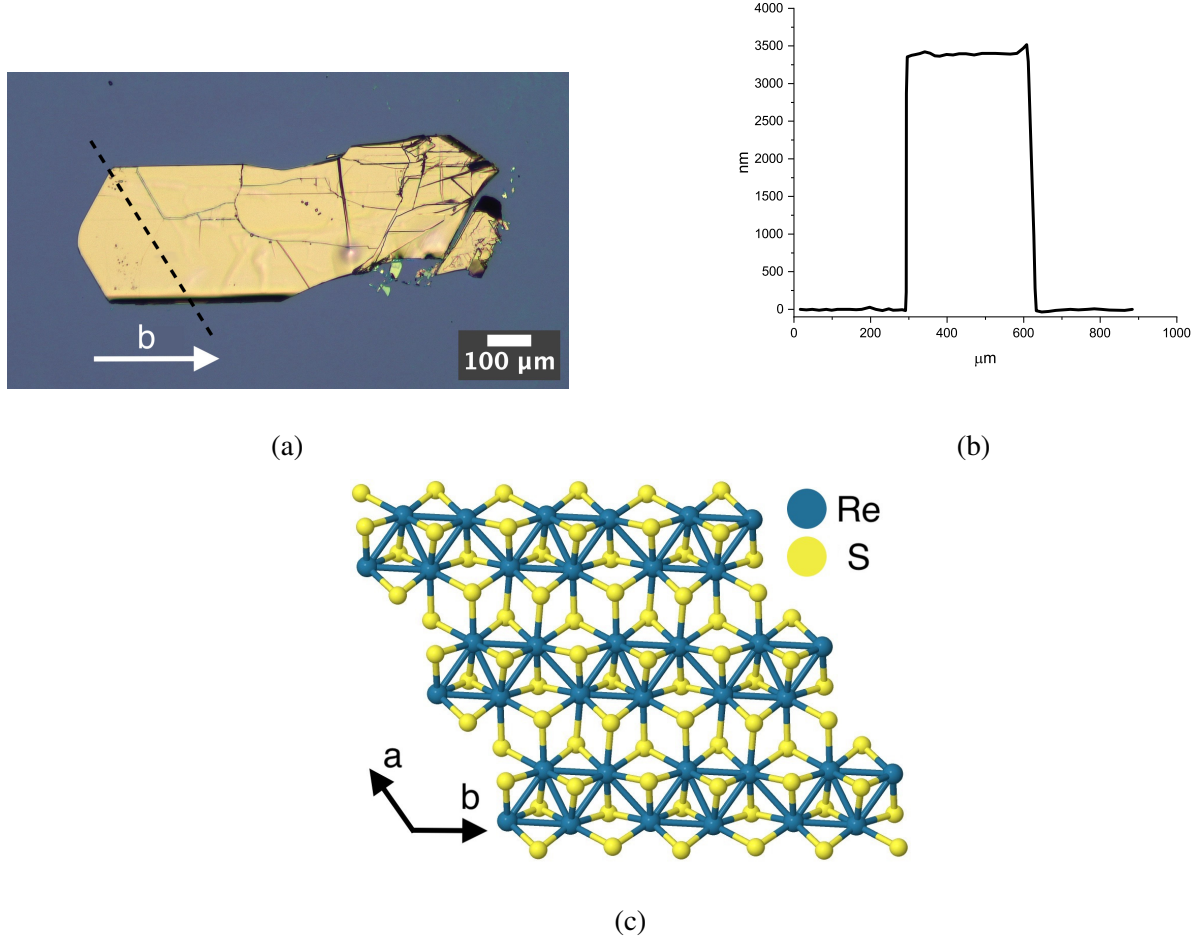
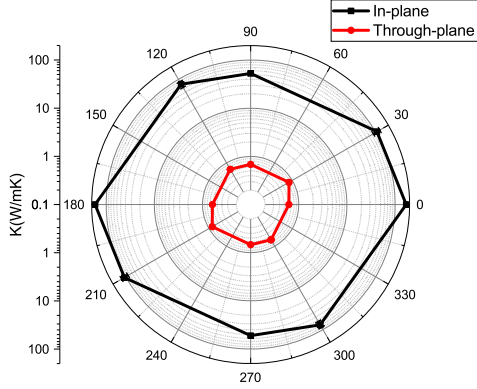
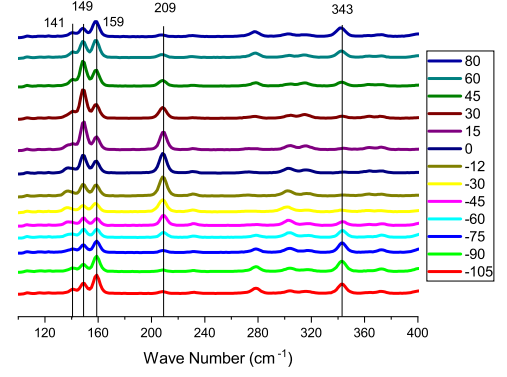


Figure 4.1: **(a)** Optical microscope image of a ReS<sub>2</sub> flake. **(b)** Optical profilometry thickness measurement of the ReS<sub>2</sub> flake in (a) across the line shown. **(c)** Crystal structure of ReS<sub>2</sub>.

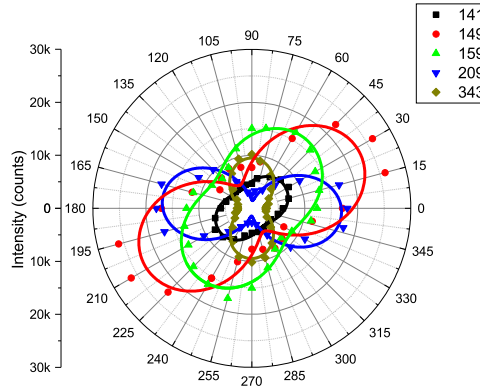




(d)

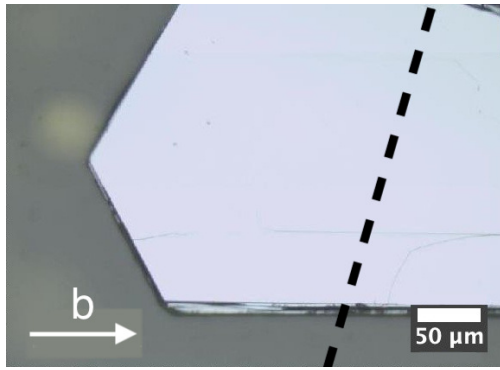


(e)

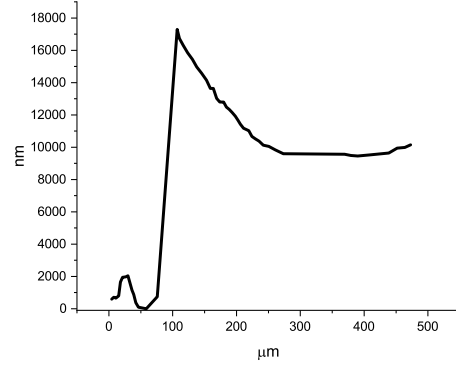


(f)

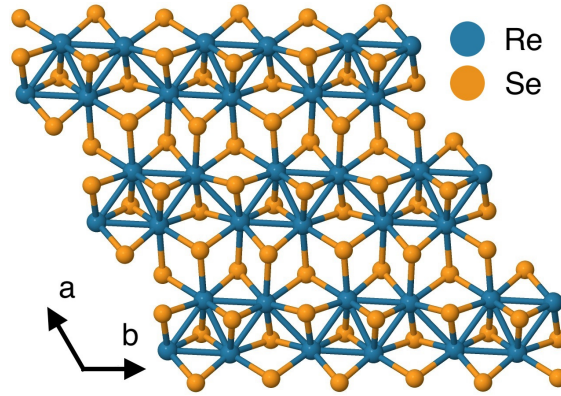
Figure 4.1: **(d)** In-plane and through-plane thermal conductivity of  $\text{ReS}_2$  for different angles. The  $0^\circ$  axis is aligned with the bottom edge of the flake in (a). **(e)** Polarized Raman spectroscopy of the  $\text{ReS}_2$  flake for different rotations of the crystal with the  $0^\circ$  angle aligning the bottom edge of the flake in (a) to the polarization axis of the Raman laser. **(f)** Polar plot of the Raman intensities for the 5 dominant modes of  $\text{ReS}_2$  shown in (e).



(a)



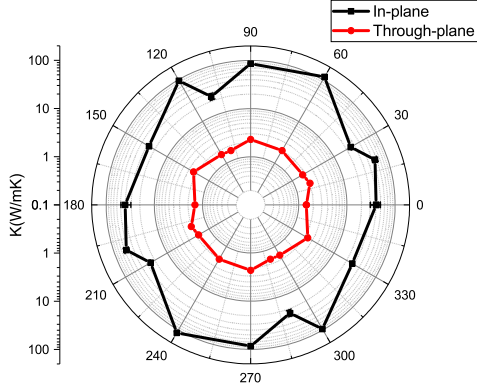
(b)



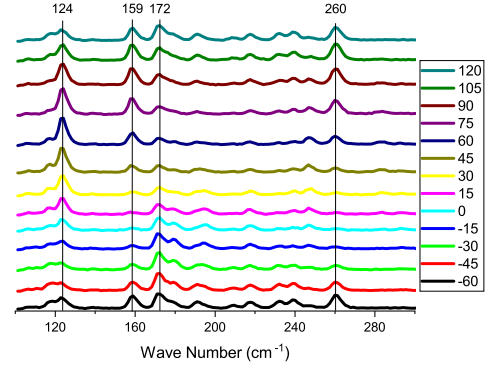
(c)

Figure 4.2: **(a)** Optical microscope image of a  $\text{ReSe}_2$  flake. **(b)** Optical profilometry thickness measurement of the  $\text{ReSe}_2$  flake in (a) across the line shown. **(c)** Crystal structure of  $\text{ReSe}_2$ .

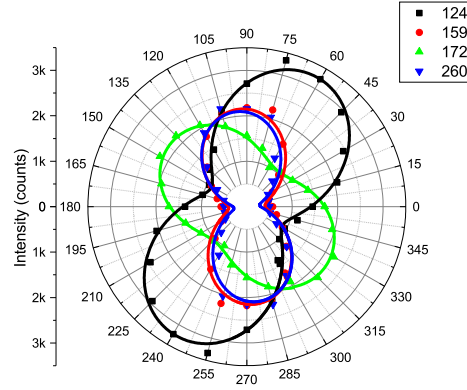
## 4.2 SAMPLE PREPARATION AND CHARACTERIZATION



(d)



(e)



(f)

Figure 4.2: **(d)** In-plane and through-plane thermal conductivity of  $\text{ReSe}_2$  for different angles. The  $0^\circ$  axis is aligned with the bottom edge of the flake in (a). **(e)** Polarized Raman spectroscopy of the  $\text{ReSe}_2$  flake for different rotations of the crystal with the  $0^\circ$  angle aligning the bottom edge of the flake in (a) to the polarization axis of the Raman laser. **(f)** polar plot of the Raman intensities for the 4 dominant modes of  $\text{ReSe}_2$  shown in (e).

### 4.3 Model Parameters and Sensitivity Analysis

The parameters used in the codes for the properties of each layer of the samples are listed in the following tables 4.1 and 4.2 with the corresponding source of each item.

Layer	Aluminium	Boundary	ReS2	ref.
$K_{zz}$ (W/mK) or $G$ (MW/m <sup>2</sup> K)	243	15	*	[9, 56]
$K_{xx}$ (W/mK)	45		*	4-point probe
$K_{yy}$ (W/mK)	45		*	4-point probe
$C$ (MJ/m <sup>3</sup> K)	2.42		2.06	[9, 57]
$t$ (nm)	52		3,000	Picosecond acoustics, Optical profilometer

Table 4.1: List of parameters used in the model for ReS<sub>2</sub>

Layer	Aluminium	Boundary	ReSe2	ref
$K_{zz}$ (W/mK) or $G$ (MW/m <sup>2</sup> K)	243	15	*	[9, 56]
$K_{xx}$ (W/mK)	73		*	4-point probe
$K_{yy}$ (W/mK)	73		*	4-point probe
$C$ (MJ/m <sup>3</sup> K)	2.42		2.06	[9, 57]
$t$ (nm)	64		10,000	Picosecond acoustics, Optical profilometer

Table 4.2: List of parameters used in the model for ReSe<sub>2</sub>

The \* in the tables above represent the values to be fitted. The best fit values do not depend on the initial guesses. No other layers are considered beneath the TMDs, as their thickness is so large that the thermal waves in the experiment do not penetrate beyond the crystals. Thus the presence

of the substrate in the model is inconsequential in this work. The references containing specific measurement methods refer to parameters that were experimentally determined using the techniques mentioned. The in-plane thermal conductivity of the Aluminium layer as an example has been evaluated utilizing 4 point probe method which measures the sheet resistance of the material that is subsequently converted to the thermal conductivity by the Wiedemann-Franz law.

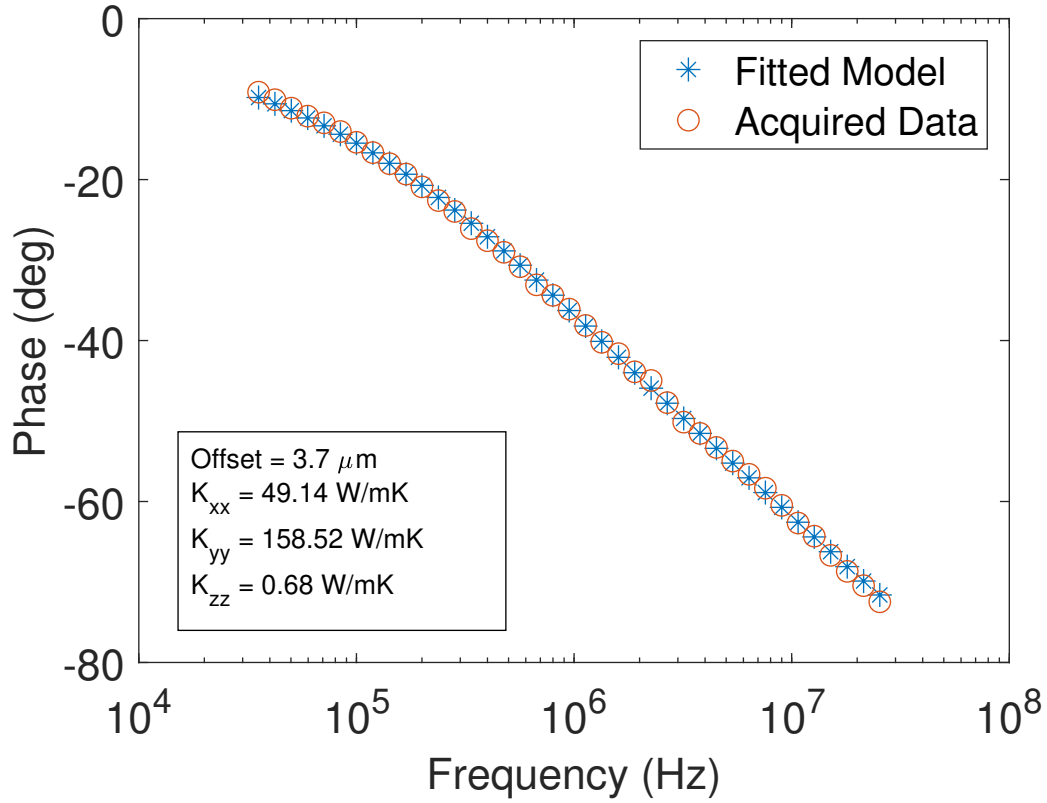


Figure 4.3: Sample model fit for ReS<sub>2</sub> @30° fitting for  $K_{xx}$ ,  $K_{yy}$ , and  $K_{zz}$

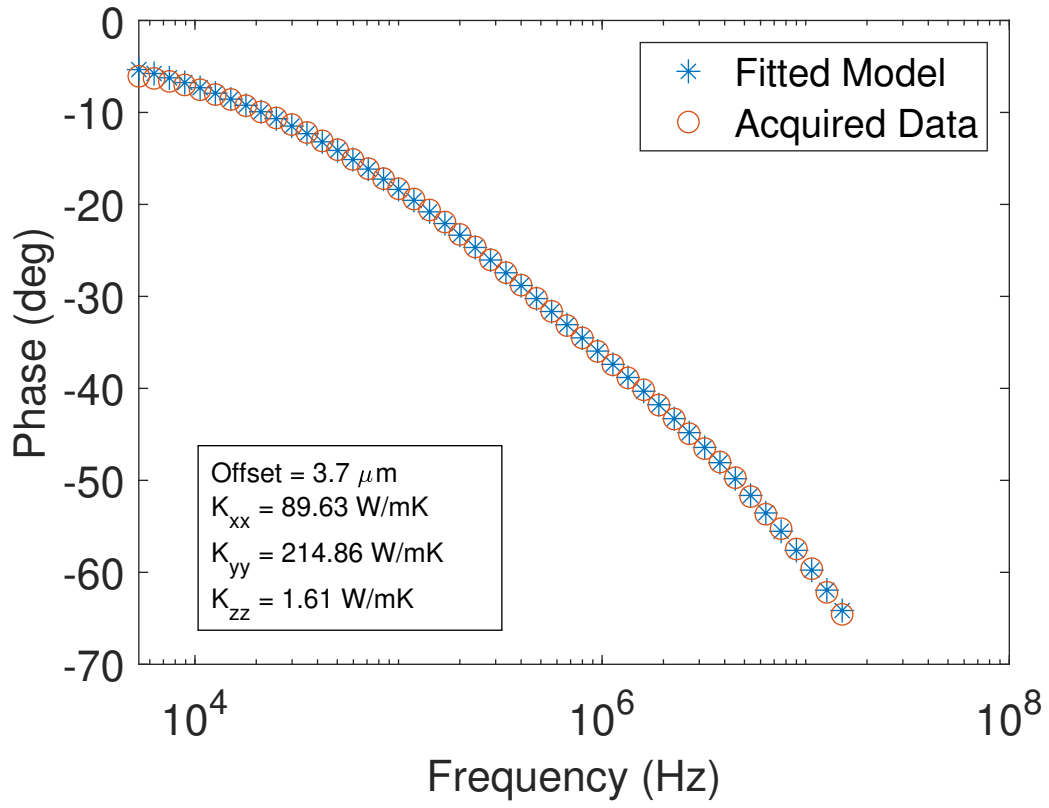


Figure 4.4: Sample model fit for  $\text{ReSe}_2$  @  $120^\circ$  fitting for  $K_{xx}$ ,  $K_{yy}$ , and  $K_{zz}$

Presented in figures 4.3 and 4.4 are graphs showing the quality of the fits for one sample measurement of each of the materials. Thermal conductivities in the x, y, and z directions are shown in the insets. As stated in one of my group's previous works [36] and in previous chapters, the sensitivity in FDTR measurements indicates how responsive the detected signal is to changes in specific parameters, such as in-plane thermal conductivity of a layer, or the radius of the pump or probe beams. This sensitivity is dependent on the thermophysical properties of the sample layers. By analyzing measurement sensitivity, it can be determined which parameters can be precisely fitted for in the model. Mathematically, the sensitivity of the measured phase signal  $\theta$  with respect to a change in parameter  $x$  is expressed as:

$$S = \frac{d\theta}{d \ln x} \quad (4.2)$$

The sensitivity curves of the  $\text{ReS}_2$  and  $\text{ReSe}_2$  are brought here as an example to demonstrate the role of each parameter in the measurements and the properties of the material that can be fitted for. These are shown in Figures 4.5, 4.6, 4.7, 4.8, 4.9, and 4.10.

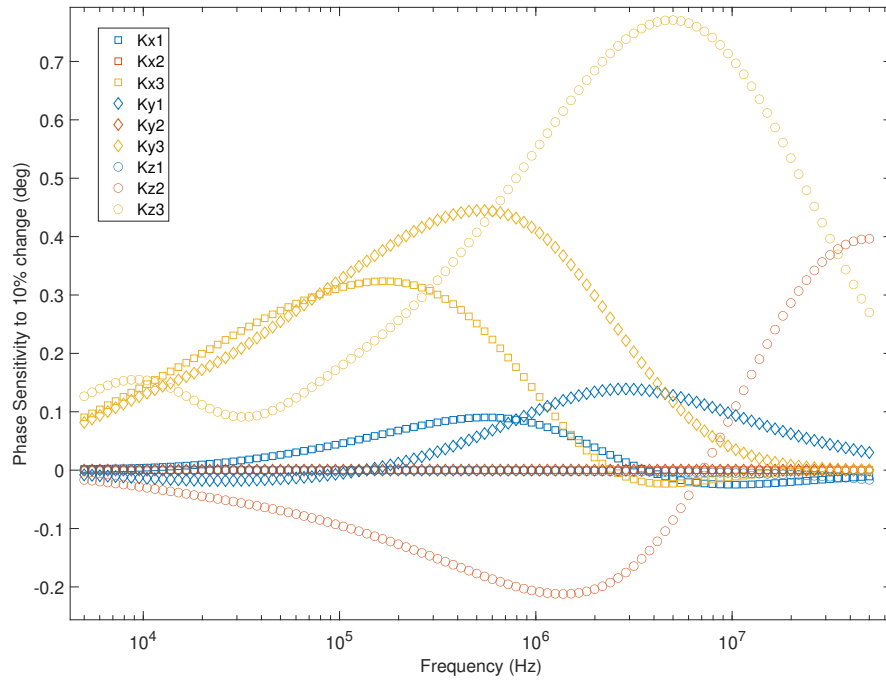


Figure 4.5: Thermal Conductivity Sensitivity analysis for  $\text{ReS}_2$ . x, y, and z refer to the direction of thermal conductivity and the numbers represent the layer as described in Table 4.1.



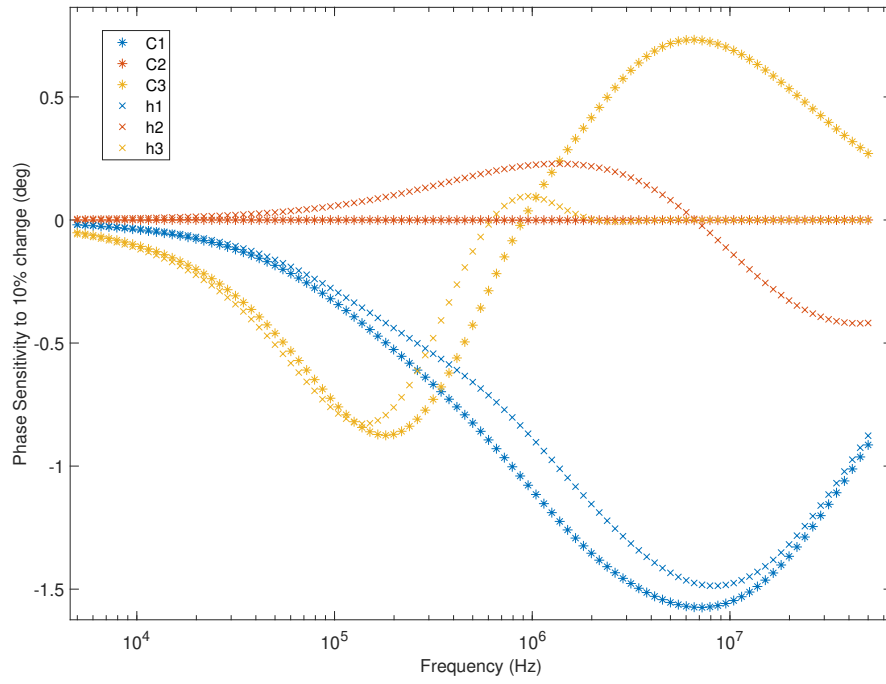


Figure 4.6: Variables Sensitivity analysis for  $\text{ReS}_2$ . C refers to the volumetric heat capacity of each layer denoted by the numbers and h represents the thickness of each layer as described in Table 4.1.

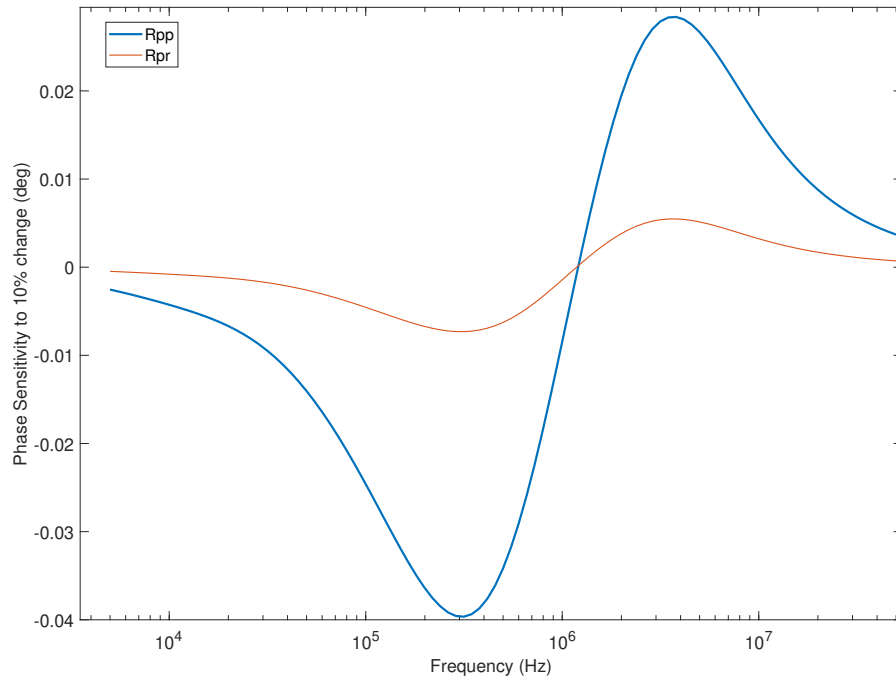


Figure 4.7: Spot Size Sensitivity analysis for ReS<sub>2</sub> with R<sub>pp</sub> being the radius of the pump beam and R<sub>pr</sub> the radius of the probe beam.

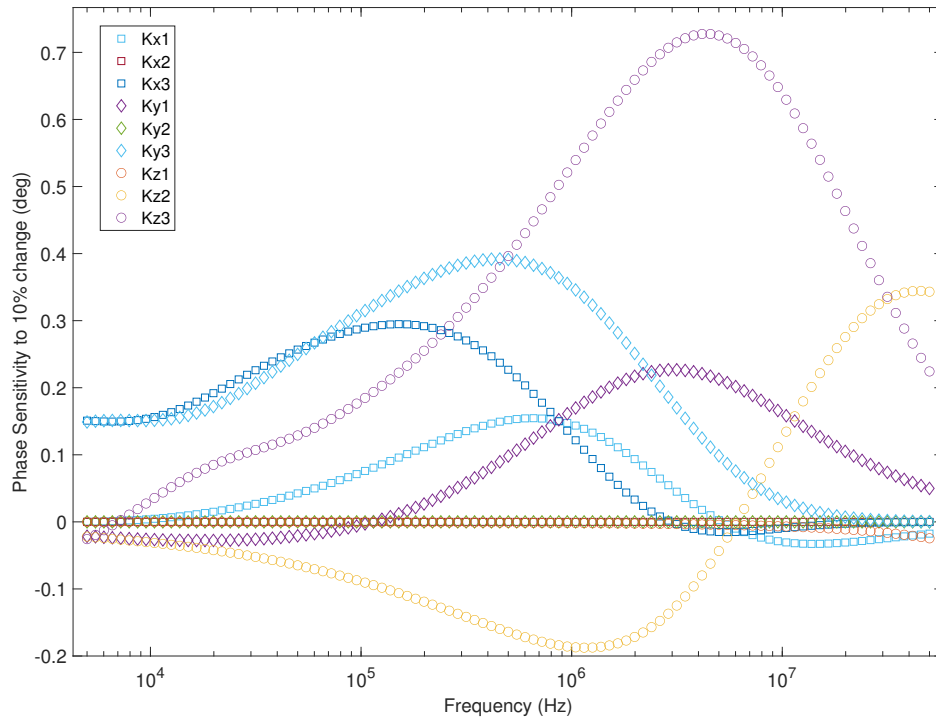


Figure 4.8: Thermal Conductivity Sensitivity analysis for  $\text{ReSe}_2$ . x, y, and z refer to the direction of thermal conductivity and the numbers represent the layer as described in Table 4.2.

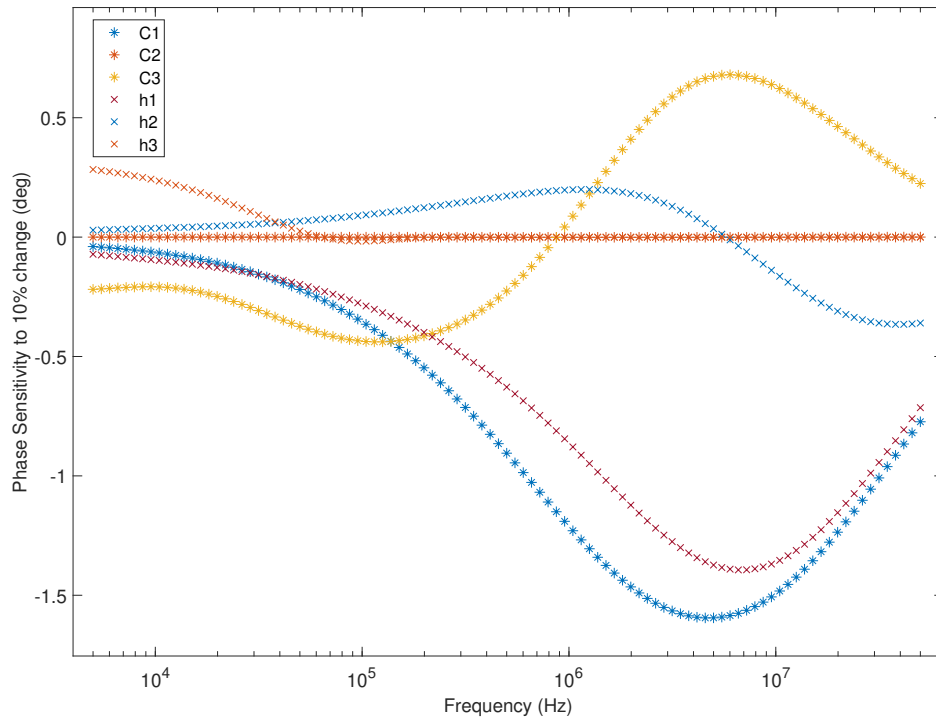


Figure 4.9: Variables Sensitivity analysis for  $\text{ReSe}_2$ . C refers to the volumetric heat capacity of each layer denoted by the numbers and h represents the thickness of each layer as described in Table 4.2.

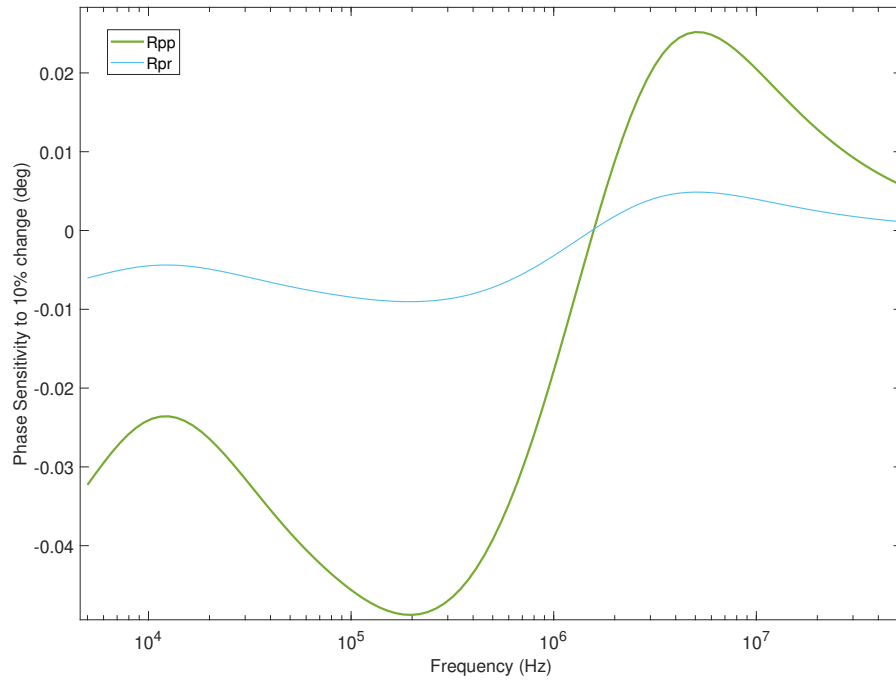


Figure 4.10: Spot Size Sensitivity analysis for ReSe<sub>2</sub> with R<sub>pp</sub> being the radius of the pump beam and R<sub>pr</sub> the radius of the probe beam.

## 4.4 Results

Figures 4.1e and 4.1f reveal a clear angular dependence in the intensity of the Raman peaks with respect to the direction of the crystal, as previously reported [54, 58]. The flakes have been aligned such that the  $0^\circ$  angle in plots correlates with the horizontal edge of the flakes as seen in Figure 4.1a. The longer horizontal edges have been shown to be likely directions on the  $b$ -axis of the crystal, due to preferential cleaving along that direction [59]. This general observation is verified by analysis of the Raman peaks, as the peaks of specific Raman modes have highest intensity when the Raman polarization direction is aligned with one of the principal axes of the crystal. For example, mode  $V$  at  $209\text{ cm}^{-1}$  has been shown to be most intense when the laser polarization is aligned with the  $b$ -axis of the  $\text{ReS}_2$  crystal [54, 58, 60, 61]. The relative angular orientation of mode  $III$  at  $149\text{ cm}^{-1}$  with respect to mode  $V$  indicates that the  $c$ -axis of the crystal is pointing down towards the substrate (the two faces of the crystal are not equivalent because of the low crystal symmetry) [54]. Based on these observations, the  $b$ -axis is assigned to  $0^\circ$  (horizontal direction) in Figure 4.1. The Raman spectra observed in this study present well-defined peaks at the expected positions for the material, suggesting a highly ordered structure typical of single-crystal domains. Moreover, the Raman spectra do not exhibit additional, unexpected peaks which would be indicative of polycrystalline domains or a high density of defects. The sharpness of the peaks and the lack of extra modes suggest that any grain boundaries present are large enough that they do not significantly affect the Raman signal. This implies that the crystalline regions in the samples are extensive and that any grain boundaries do not lead to noticeable scattering or defects that would disturb the Raman measurements. Thus, the samples are believed to be largely defect-free, with grain boundaries that are sufficiently large as

to not impede the thermal transport properties that are being investigated.

The measurements reveal a notable anisotropy in the in-plane thermal conductivity  $K_r(\theta)$  of the examined flakes, with highest values obtained along the  $b$ -axis (along the Re atomic chain direction), as previously observed by Jang [9]. The value recorded for  $K_r(\theta - 0^\circ) = 169 \pm 11$  W/mK is substantially higher than the values recorded by Jang, but the value for  $K_r(\theta - 90^\circ) = 53 \pm 4$  W/mK is the same within error. The high conductivity value is also found in other ReS<sub>2</sub> flakes that were tested, and can potentially be ascribed to procuring the crystals from different sources, which can lead to differences in crystal grain size [62–64]. Indeed, in spite of large lateral grain sizes spanning hundreds of  $\mu\text{m}$  along the basal plane, the continuity of the crystal in the through-plane direction can be interrupted by grain boundaries or stacking faults. Such sources of boundary scattering can, similarly to limitations in the thickness of the crystal itself, play an important role in limiting  $K_r$  and  $K_z$  [64, 65]. Although Jang did not find variations in  $K$  for sample thickness ranging from 60 to 450 nm, the difference with my results may be ascribed to the presence of defects on a length scale of a few tens of nm.

The measured variation in  $K_r(\theta)$  reveals an extremely large in-plane thermal conductivity anisotropy ratio of 3.2. In the context of TMDs [66] and 2D materials [67, 68], it is not unprecedented to observe such high values of  $K_r$  and large anisotropies between  $K_r$  and  $K_z$ . However, large variations in  $K_r(\theta)$ , that is *within* the basal plane, are less common. Black phosphorous was found to have an in-plane anisotropy of 2 [69], and so did TiS<sub>3</sub> [70]. However, I am not aware of experimental observations with in-plane anisotropies as large as the ones reported here. The thermal conductivities of MXenes [71–73] have been predicted to have larger in-plane anisotropies. In the

paper by Luo et al. [71], the thermal conductivity of  $\text{Sc}_3(\text{CN})\text{F}_2$  is calculated to have values of 283 and 111 W/mK along different in-plane directions, leading to an in-plane anisotropy ratio of 2.55. I am not aware of such values of in-plane anisotropy being experimentally verified. Therefore, the in-plane anisotropy ratio of 3.2 found for  $\text{ReS}_2$  appears to be a record.

The value for the through-plane conductivity  $K_z$  is 0.66 W/mK, and in agreement with the previous results of Jang [9]. Such a low value is in itself remarkable and it has been attributed to the very weak interlayer bonding along the  $c$ -axis of  $\text{ReS}_2$ . The differences in in-plane and through-plane  $K$  leads to a ratio of 256, which almost as high as that of graphite.

The results for  $\text{ReSe}_2$  presented in Figure 4.2 show even more intriguing features. The Raman spectra makes it possible to identify the crystal axis orientation, which again is presented here by having the Rhenium atomic chains along the  $b$ -axis being referred to  $\theta = 0^\circ$  [54, 74]. Unlike  $\text{ReS}_2$ , there is no prominent Raman peak that is aligned with the  $b$ -axis, but rather it is located  $60^\circ$  and  $90^\circ$  from modes  $IV$  ( $124 \text{ cm}^{-1}$ ) and  $V$  ( $159 \text{ cm}^{-1}$ ), respectively. Also unlike  $\text{ReS}_2$ , the maximum value recorded for  $K_r(\theta)$  is  $60^\circ$  away from the  $b$ -axis, and along mode  $IV$  in the polarized Raman data. The correlation between maximum value of  $K_r(\theta)$  with a prominent Raman peak, which occurs along the  $b$ -axis for  $\text{ReS}_2$  but not for  $\text{ReSe}_2$ , strongly suggests that the thermal transport anisotropy is linked to the different phonon band structure on these materials, which in turn is determined by their crystal structure. Although these Rhenium-based TMDs have a similar crystal structure, it appears that small but important variations have marked effect on the thermal transport.  $\text{ReSe}_2$  exhibits generally lower value for  $K_r$ , and this could be attributed to the larger atomic mass of selenium compared to sulfur [8], though the effect of crystal quality cannot be ruled out which might be



responsible for the variation in reported thermal conductivity of  $\text{ReS}_2$ . The in-plane anisotropy ratio is found to be even higher than  $\text{ReS}_2$  at 4.3, whereas the value of  $K_z$  is higher. The origin of the larger value for  $K_z$  or the lack of monotonic variation in the recorded  $K_r(\theta)$  between its maximum and minimum values are not currently known. It will be important to carry out theoretical modeling of the heat transport in these structures to better relate crystal and thermal properties in light of this data. As a sanity check for the tests, 68% and 95% confidence intervals are calculated for two points for each of the materials. The corresponding graphs can be seen in figures 4.11, 4.12, 4.13, and 4.14.

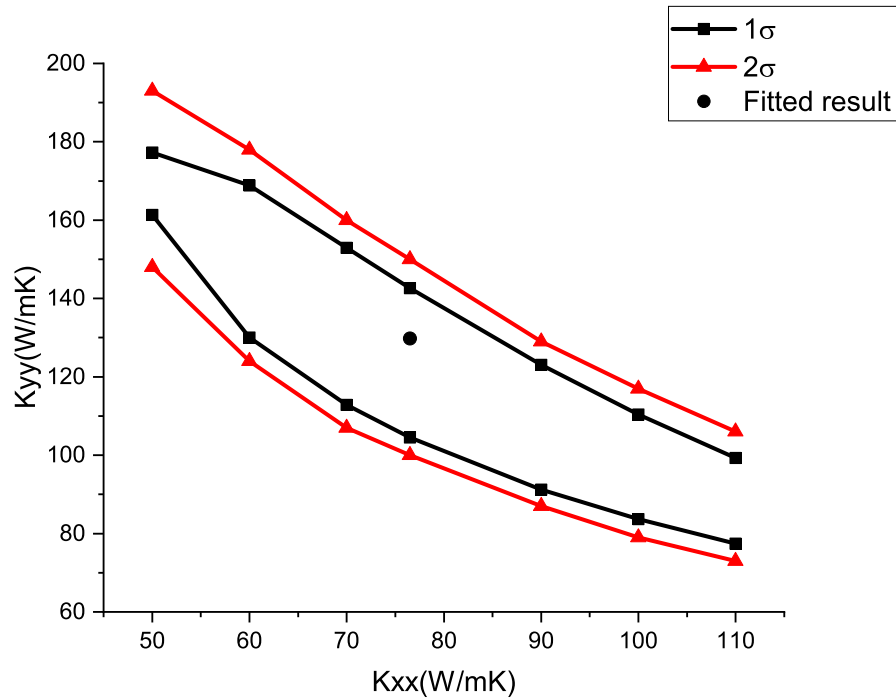


Figure 4.11: Analysis of fitted parameter dependency for  $\text{ReS}_2$  at  $0^\circ$  orientation alongside the 68% and 95% confidence intervals for the obtained measurement.

Also, to ensure the FDTR setup and the model behave as expected, a reference sample of

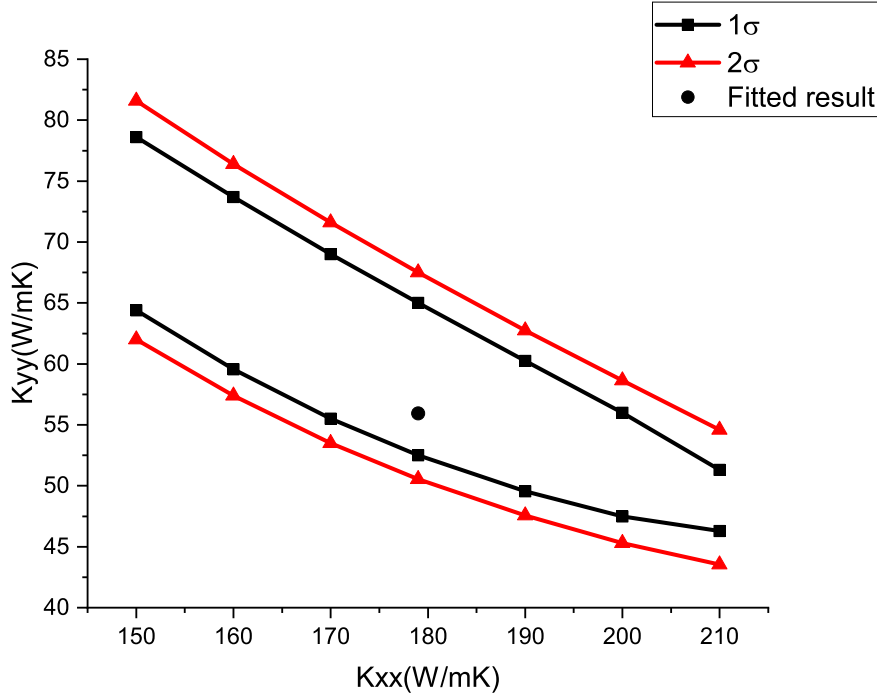


Figure 4.12: Analysis of fitted parameter dependency for ReS<sub>2</sub> at 120° orientation alongside the 68% and 95% confidence intervals for the obtained measurement.

Al/SiO<sub>2</sub>/Si with a known SiO<sub>2</sub> thickness of 150nm has been measured on the setup as a calibration test. The results can be seen in figure 4.15 with the fitted thickness for the SiO<sub>2</sub> layer of 151nm with the standard error of 5nm. To ensure the repeatability of the results, some angles have been measured twice. For instance, the ReSe<sub>2</sub> sample was initially measured at 0° to have  $K_{xx}$  of  $47.87 \pm 18.57$  W/mK and  $K_{yy}$  of  $13.83 \pm 7.33$  W/mK. A subsequent measurement yielded values of  $K_{xx} = 45.56 \pm 21.69$  W/mK and  $K_{yy} = 15.38 \pm 9.50$  W/mK. The second set of results is in close agreement with the first, thereby underscoring the repeatability of the measurements and reinforcing the reliability of the data.

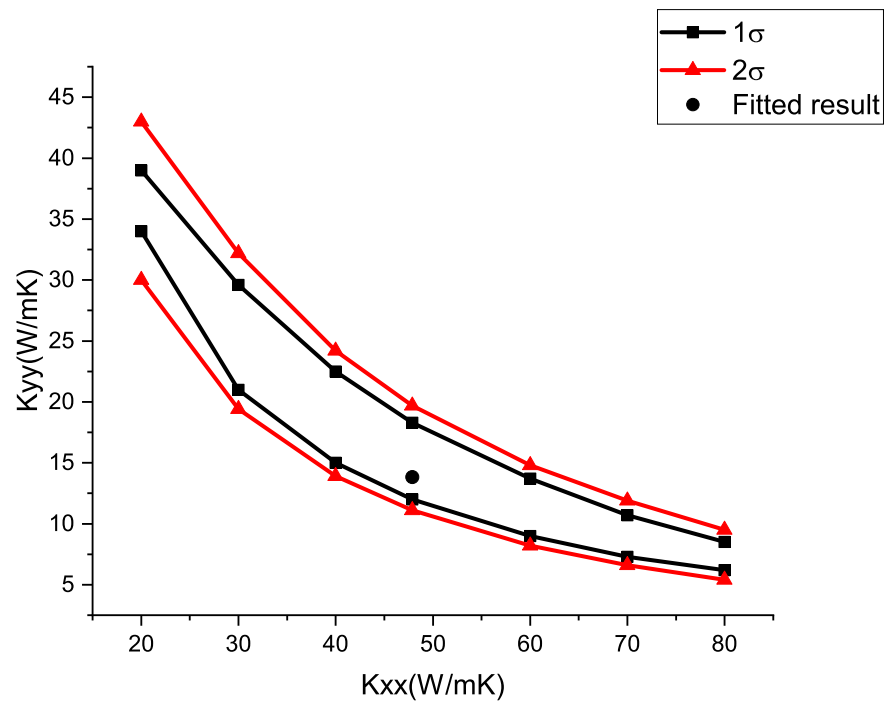


Figure 4.13: Analysis of fitted parameter dependency for  $\text{ReSe}_2$  at  $0^\circ$  orientation alongside the 68% and 95% confidence intervals for the obtained measurement.

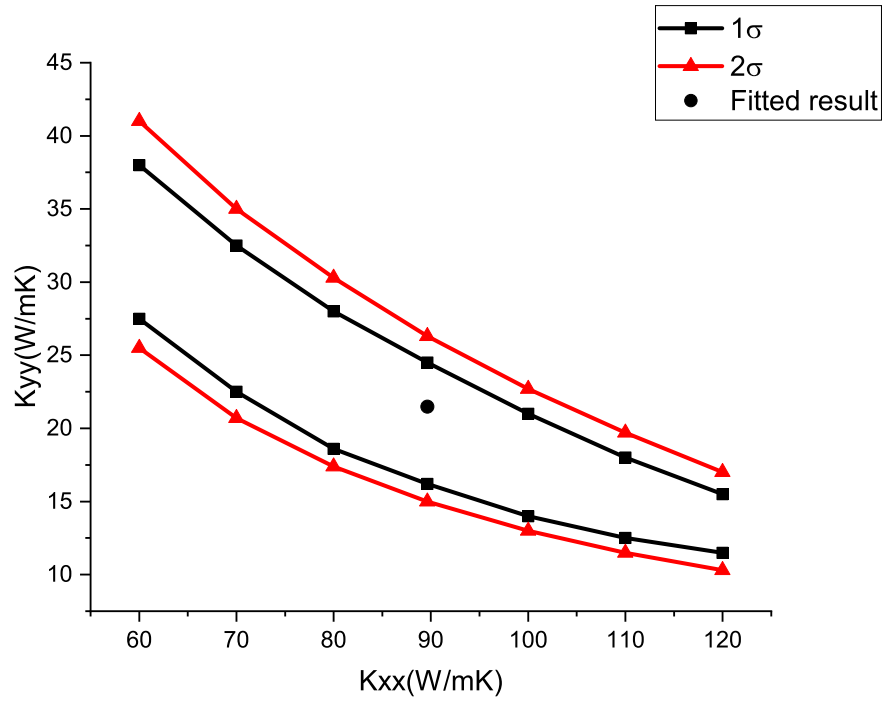
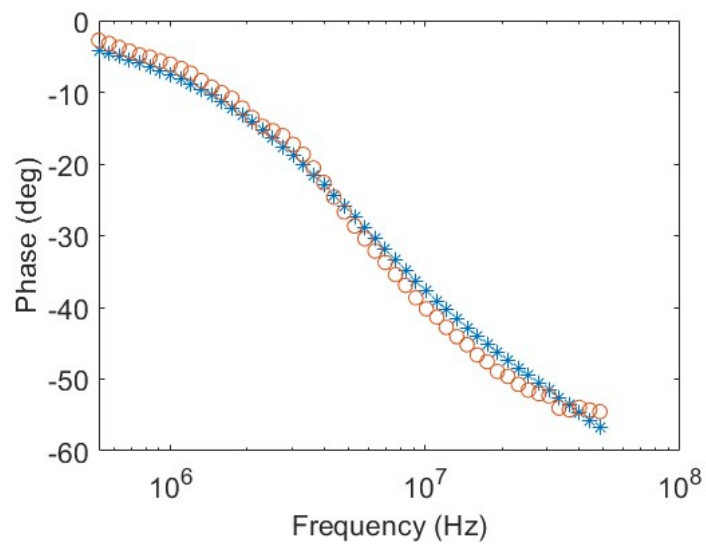


Figure 4.14: Analysis of fitted parameter dependency for ReSe<sub>2</sub> at 120° orientation alongside the 68% and 95% confidence intervals for the obtained measurement.

```
ans =  
  
1.514841141311439e-07  
  
se =  
  
5.086955398203153e-09
```

(a)



(b)

Figure 4.15: Calibration test fitting for the thickness of the SiO<sub>2</sub> layer in the Al/SiO<sub>2</sub>/Si sample with a known thickness of 150nm.

# Chapter 5

## Conclusion

In conclusion, this study provides significant insights into the thermal properties of Rhenium-based transition metal dichalcogenides (TMDs), specifically  $\text{ReS}_2$  and  $\text{ReSe}_2$ , which until now remained relatively underexplored with  $\text{ReSe}_2$  having no known experimental measurements on the thermal conductivity. The results underscore an extremely high in-plane anisotropy for both  $\text{ReS}_2$  and  $\text{ReSe}_2$ , a characteristic that distinguishes these materials from other TMDs and 2D materials more broadly. While  $\text{ReS}_2$  and  $\text{ReSe}_2$  share several common features such as high in-plane anisotropy and low through-plane thermal conductivity in general, their differences have been highlighted including the values for through-plane thermal conductivities and the angles at which the maximum in-plane thermal conductivities happen which could be due to small differences in their crystal structure. Furthermore, the implementation of a tensor-based thermal conductivity representation specifically adapted for use in FDTR systems utilized in the computational approach, coupled with differential x-y offsets, provides a more accurate picture of these intriguing materials' thermal properties. This

conclusion aligns with existing literature on the thermal conductivities of other TMDs, reinforcing the validity of the findings. The findings herein open the door for further investigation into these unique materials and their potential applications in the realm of nanotechnology and semiconductor devices such as fabrication of photodetectors or energy harvesting devices. The anisotropy of ReS<sub>2</sub> has been used to create polarization sensitive photodetectors as an example [75]. Also, owing to the fact that these materials have low through-plane thermal conductivities, they have potential applications in creating thermoelectric devices where the hot and cold sides need to be isolated from each other. Future studies should continue to explore these and other under-studied TMDs to uncover their full potential in the aforementioned areas and the range of their distinct properties. Analyzing the effect of various intrinsic and extrinsic factors such as defects, grain boundaries, and layer number on thermal transport in TMDs will build upon the insights outlined in this thesis. These studies can also further supported by performing theoretical calculations along with experimental studies of these effects.

# References

- [1] Manzeli S, Ovchinnikov D, Pasquier D, Yazyev O V and Kis A 2017 *Nature Reviews Materials* **2** 1–15
- [2] Choi W, Choudhary N, Han G H, Park J, Akinwande D and Lee Y H 2017 *Materials Today* **20** 116–130
- [3] Zhang G and Zhang Y W 2017 *Journal of Materials Chemistry C* **5** 7684–7698
- [4] Lu Z, Neupane G P, Jia G, Zhao H, Qi D, Du Y, Lu Y and Yin Z 2020 *Advanced Functional Materials* **30** 2001127
- [5] Mortazavi B, Quey R, Ostadhossein A, Villani A, Moulin N, van Duin A C and Rabczuk T 2017 *Applied Materials Today* **7** 67–76
- [6] Muratore C, Varshney V, Gengler J J, Hu J, Bultman J E, Smith T M, Shamberger P J, Qiu B, Ruan X, Roy A K *et al.* 2013 *Applied Physics Letters* **102** 081604
- [7] Ma J, Li W and Luo X 2016 *Applied Physics Letters* **108** 082102



- [8] Zhang Z, Xie Y, Ouyang Y and Chen Y 2017 *International Journal of Heat and Mass Transfer* **108** 417–422
- [9] Jang H, Ryder C R, Wood J D, Hersam M C and Cahill D G 2017 *Advanced Materials* **29** 1700650
- [10] Tongay S, Sahin H, Ko C, Luce A, Fan W, Liu K, Zhou J, Huang Y S, Ho C H, Yan J *et al.* 2014 *Nature communications* **5** 1–6
- [11] Mahmoud M M and Joubert D P 2018 *Materials Today: Proceedings* **5** 10424–10430
- [12] Bang J, Park O, Kim H S, Hwang S M, Lee S W, Park S J, Kim S i *et al.* 2023 *International Journal of Energy Research* **2023**
- [13] Chen G 2005 *Nanoscale energy transport and conversion: a parallel treatment of electrons, molecules, phonons, and photons* (Oxford university press)
- [14] Hopkins P E 2013 *International Scholarly Research Notices* **2013**
- [15] Tritt T M 2005 *Thermal conductivity: theory, properties, and applications* (Springer Science & Business Media)
- [16] Cahill D G, Ford W K, Goodson K E, Mahan G D, Majumdar A, Maris H J, Merlin R and Phillpot S R 2003 *Journal of applied physics* **93** 793–818
- [17] Kaul A B 2014 *Journal of Materials Research* **29** 348–361
- [18] Pop E 2010 *Nano Research* **3** 147–169

- [19] Gu X, Wei Y, Yin X, Li B and Yang R 2018 *Reviews of Modern Physics* **90** 041002
- [20] Mukherjee B, Hayakawa R, Watanabe K, Taniguchi T, Nakaharai S and Wakayama Y 2021 *Advanced Electronic Materials* **7** 2000925
- [21] Zhang E, Jin Y, Yuan X, Wang W, Zhang C, Tang L, Liu S, Zhou P, Hu W and Xiu F 2015 *Advanced Functional Materials* **25** 4076–4082
- [22] Geim A K 2009 *science* **324** 1530–1534
- [23] Mas-Balleste R, Gomez-Navarro C, Gomez-Herrero J and Zamora F 2011 *Nanoscale* **3** 20–30
- [24] Gupta A, Sakthivel T and Seal S 2015 *Progress in Materials Science* **73** 44–126
- [25] Yin Z, Li H, Li H, Jiang L, Shi Y, Sun Y, Lu G, Zhang Q, Chen X and Zhang H 2012 *ACS nano* **6** 74–80
- [26] Cahill D G 2004 *Review of scientific instruments* **75** 5119–5122
- [27] Schmidt A J, Chen X and Chen G 2008 *Review of Scientific Instruments* **79** 114902
- [28] Zhao D, Qian X, Gu X, Jajja S A and Yang R 2016 *Journal of Electronic Packaging* **138** 040802
- [29] Cahill D G 1990 *Review of scientific instruments* **61** 802–808
- [30] Healy J, De Groot J and Kestin J 1976 *Physica B+ c* **82** 392–408
- [31] Parker W, Jenkins R, Butler C and Abbott G 1961 *Journal of applied physics* **32** 1679–1684

- [32] Hopkins P E, Serrano J R, Phinney L M, Kearney S P, Grasser T W and Harris C T 2010
- [33] Shahzadeh M, Rahman M, Hellwig O and Pisana S 2018 *Review of Scientific Instruments* **89**
- [34] Regner K T, Sellan D P, Su Z, Amon C H, McGaughey A J and Malen J A 2013 *Nature communications* **4** 1640
- [35] Rahman M, Davey K and Qiao S Z 2017 *Advanced Functional Materials* **27** 1606129
- [36] Rahman M, Shahzadeh M, Braeuninger-Weimer P, Hofmann S, Hellwig O and Pisana S 2018 *Journal of Applied Physics* **123** 245110
- [37] Rahman M, Shahzadeh M and Pisana S 2019 *Journal of Applied Physics* **126**
- [38] Feldman A *et al.* 1999 *High Temperatures-High Pressures* **31** 293–298
- [39] Gundrum B C, Cahill D G and Averback R S 2005 *Physical Review B* **72** 245426
- [40] Schmidt A J, Cheaito R and Chiesa M 2009 *Review of scientific instruments* **80** 094901
- [41] Yang J, Ziade E, Maragliano C, Crowder R, Wang X, Stefancich M, Chiesa M, Swan A K and Schmidt A J 2014 *Journal of Applied Physics* **116** 023515
- [42] Liu J, Zhu J, Tian M, Gu X, Schmidt A and Yang R 2013 *Review of Scientific Instruments* **84** 034902
- [43] URL <https://sites.udel.edu/feserlab/tdtr-analysis-tools/>
- [44] Feser J P and Cahill D G 2012 *Review of Scientific Instruments* **83** 104901

- [45] Schmidt A J, Cheaito R and Chiesa M 2010 *Journal of Applied Physics* **107** 024908
- [46] Yang J, Maragliano C and Schmidt A J 2013 *Review of Scientific Instruments* **84** 104904
- [47] Tang L and Dames C 2021 *International Journal of Heat and Mass Transfer* **164** 120600
- [48] Feser J P, Liu J and Cahill D G 2014 *Review of Scientific Instruments* **85** 104903
- [49] Li Y, Kuang G, Jiao Z, Yao L and Duan R 2022 *Materials Research Express*
- [50] Magda G Z, Pető J, Dobrik G, Hwang C, Biró L P and Tapasztó L 2015 *Scientific reports* **5** 14714
- [51] Watson A J, Lu W, Guimarães M H and Stöhr M 2021 *2D Materials* **8** 032001
- [52] Li Y, Xie X, Li B, Sun X, Yang Y, Liu J, Feng J, Zhou Y, Li Y, Liu W *et al.* 2022 *Nanoscale* **14** 7484–7492
- [53] Ooi S and Ahmad H 2022 *Optical Materials* **128** 112363
- [54] Choi Y, Kim K, Lim S Y, Kim J, Park J M, Kim J H, Lee Z and Cheong H 2020 *Nanoscale Horizons* **5** 308–315
- [55] Hafeez M, Gan L, Bhatti A S and Zhai T 2017 *Materials Chemistry Frontiers* **1** 1917–1932
- [56] Committee A H *et al.* 1990 *ASM handbook* **2** 62–122
- [57] Takahashi Y, Azumi T and Sekine Y 1989 *Thermochimica acta* **139** 133–137
- [58] Zhang S, Mao N, Zhang N, Wu J, Tong L and Zhang J 2017 *ACS nano* **11** 10366–10372

- [59] Wang H, Liu E, Wang Y, Wan B, Ho C H, Miao F and Wan X 2017 *Physical Review B* **96** 165418
- [60] Chenet D A, Aslan B, Huang P Y, Fan C, Van Der Zande A M, Heinz T F and Hone J C 2015 *Nano letters* **15** 5667–5672
- [61] Hart L, Dale S, Hoye S, Webb J L and Wolverson D 2016 *Nano letters* **16** 1381–1386
- [62] Li Z, Liu Y, Lindsay L, Xu Y, Duan W and Pop E 2017 *arXiv preprint arXiv:1711.02772*
- [63] Lindroth D O and Erhart P 2016 *Physical Review B* **94** 115205 URL <https://link.aps.org/doi/10.1103/PhysRevB.94.115205>
- [64] Rahman M, Parvez K, Fugallo G, Dun C, Read O, Alieva A, Urban J J, Lazzeri M, Casiraghi C and Pisana S 2022 *Nanomaterials* **12** ISSN 2079-4991 URL <https://www.mdpi.com/2079-4991/12/21/3861>
- [65] Xiao P, Chavez-Angel E, Chaitoglou S, Sledzinska M, Dimoulas A, Sotomayor Torres C M and El Sachat A 2021 *Nano Lett.* **21** 9172–9179 ISSN 1530-6984 URL <https://doi.org/10.1021/acs.nanolett.1c03018>
- [66] Kim S E, Mujid F, Rai A, Eriksson F, Suh J, Poddar P, Ray A, Park C, Fransson E, Zhong Y *et al.* 2021 *Nature* **597** 660–665
- [67] Cahill D G 2012 *MRS bulletin* **37** 855–863
- [68] Yang J, Liu C, Xie H and Yu W 2021 *Nanotechnology* **32** 162001

- [69] Luo Z, Maassen J, Deng Y, Du Y, Garrelts R P, Lundstrom M S, Ye P D and Xu X 2015 *Nature Communications* **6** 8572 ISSN 2041-1723 URL <https://doi.org/10.1038/ncomms9572>
- [70] Liu H, Yu X, Wu K, Gao Y, Tongay S, Javey A, Chen L, Hong J and Wu J 2020 *Nano Lett.* **20** 5221–5227 ISSN 1530-6984 URL <https://doi.org/10.1021/acs.nanolett.0c01476>
- [71] Luo K, Zha X H, Zhou Y, Guo Z, Lin C T, Huang Q, Zhou S, Zhang R and Du S 2018 *RSC advances* **8** 22452–22459
- [72] Zha X H, Zhou J, Zhou Y, Huang Q, He J, Francisco J S, Luo K and Du S 2016 *Nanoscale* **8** 6110–6117
- [73] Zha X H, Huang Q, He J, He H, Zhai J, Francisco J S and Du S 2016 *Scientific reports* **6** 27971
- [74] Wolverson D, Crampin S, Kazemi A S, Ilie A and Bending S J 2014 *ACS nano* **8** 11154–11164
- [75] Liu F, Zheng S, He X, Chaturvedi A, He J, Chow W L, Mion T R, Wang X, Zhou J, Fu Q *et al.* 2016 *Advanced Functional Materials* **26** 1169–1177